Performance analysis of frictional inerter-based vibration isolator

Cui Chao[a,b], Baiyang Shi[c], Wei Dai[d], Jian Yang[a,b*][0000-0003-4255-9622]

[a]Department of Mechanical, Materials and Manufacturing Engineering, University of Nottingham Ningbo China, 199 Taikang East Road, Ningbo 315100, P.R. China

[b]International Academy of Marine Economy and Technology, University of Nottingham Ningbo China, 199 Taikang East Road, Ningbo 315100, P.R. China

[c]Department of Engineering Design and Mathematics, University of the West of England, Bristol, BS16 1QY, United Kingdom.

[d]School of Naval Architecture and Ocean Engineering, Huazhong University of Science and Technology, Luoyu Road 1037, Wuhan 430074, P.R. China

Abstract

Purpose: This study aims to gain an in-depth understanding of the effect of the inherent dry friction of inerter devices on the performance of nonlinear frictional inerter-based vibration isolation system (NFI-VIS).

Methods: The power flow analysis method is used to investigate quantitatively the internal vibration transmission and energy dissipation. The harmonic balance (HB) method with alternating frequency time (AFT) scheme is used to obtain the steady-state dynamic responses, with verification by numerical integration results.

Results: Results show that the use of the nonlinear inerter in the system can reduce the force and vibration power flow transmission over a wide frequency band. The inherent friction of the inerter can benefit vibration isolation when the excitation amplitude is large enough to overcome the inerter friction.

Conclusion: This research reveals complex nonlinear dynamic phenomena of the system emerging from the frictional inerter and shows that the inherent dry friction of the inerter should be considered in future isolator design.

Keywords: Inerter; Dry Friction; Power Dissipation; Vibration isolator; Nonlinearity; Vibration suppression

1 Introduction

Suppression of undesired vibrations is needed in many applications such as vehicle suspension systems [1], buildings [2-4], and aircraft landing gear [5]. Vibration isolation systems have been widely used and various designs have been investigated for superior performance. Salvatore *et al.* [6] studied vibration isolators combing negative stiffness elements with memory alloy materials to achieve effective broadband vibration isolation. One potential method for better vibration isolation is to use the inerter, which is a passive mechanical element for which the generated force is proportional to the relative acceleration between its two ends [7]. Linear and nonlinear inerter-based vibration isolators have been proposed to enhance vibration isolation performance [8]. Inerter can also be used in absorbers to reduce gust loads in truss-supported wings [9] and for enhancing wave damping in metamaterial beam structures [10]. A tuned inerter damper (TID) has been shown to provide good vibration absorption performance while having reduced physical weight compared to conventional tuned mass damper (TMD) [11].

Considerable work has also been carried out to investigate the influence of adding an inerter on a dynamic system. Wang *et al.* [2] identified the benefit of inerter in building models to reduce traffic and earthquake-induced vibrations. Marian and Giaralis [12] introduced a tuned-mass-damper-inerter, with the benefit of having a lower physical mass than the conventional TMD without compromising the performance. Lazar *et al.* [13] proposed a novel passive vibration control system using a TID, demonstrating better vibration reduction. Brzeski *et al.* [14] introduced a pendulum-based absorber with a nonlinear Duffing oscillator and showed that unhoped bifurcations and instabilities for a T-shaped pendulum-tuned mass absorber can be eliminated. Many studies have shown that the incorporation of linear and nonlinear inerter-based mechanisms can improve the dynamic performance of engineering structures [15-18].

There has been a limited number of studies on inerter-based structural nonlinearity, especially on the effect of its inherent friction. Papageorgiou *et al.* [19] performed an experimental study comparing the ideal and non-ideal states of inerters. Wang and Su [20] investigated numerically and experimentally nonlinear properties of an inerter. The effect of friction on vehicle suspension performance was analyzed. Sun *et al.* [21] investigated the influence of ball-screw inerter nonlinearities on various performance indices under different suspension layouts. Based on a Coulomb friction model, Shen *et al.* investigated the influence of nonlinearities factors including friction and damping force in a fluid inerter [22]. Brezeski *et al.* [23] analyzed the dynamics of tuned-mass-dampers with an inerter. It was found that the overall efficiency of the TMD is improved at proper friction, and increasing friction caused the disappearance of the resonance peak in a frequency response curve. Mnich *et al.* [24] studied the friction of an inerter during oscillatory motion and showed that the friction of an inerter with and without a flywheel can reach as high as 40 N. The vibration transmission properties of inerter-based vibration isolation systems with internal friction have not been fully addressed.

To evaluate the effectiveness of vibration isolation systems, force / displacement transmissibility and time-averaged vibration energy transmission have been used as performance indicators [25]. Vibration power flow allows a better quantification of the transmission of the vibration within the dynamic system from an energy perspective [26]. The power flow analysis (PFA) was applied to study inerter-based nonlinear systems [27, 28]. In the study of a diamond-shaped linkage mechanism [29], the beneficial performance of nonlinear vibration isolators was investigated from the aspects of force transmission and power dissipation. There is a need for in-depth understanding of the inherent friction effects of inerters on vibration transmission and suppression [25]. As friction nonlinearity can have strong influence on system dynamics and vibration transmission [30], frictional inerter-based vibration isolation systems (NFI-VIS) should be investigated.

This study attempts to address the issues by detailed analysis into the dynamics and isolation performance of NFI-VIS. Main contributions of the current paper are: (1) a systematic investigation into the influence of the inherent friction on inerter-based vibration isolators and (2) the use of vibrational power flow variables and transmissibility to assess the influence of frictional inerters on the performance of the isolators. To study the effect of the inherent friction of inerters, single-DOF (SDOF) NFI-VIS subjected to force or base-motion excitations and 2-DOF NFI-VIS are considered. It is shown that the frequency band of effective isolation is broadened by using the NFI-VIS. It is also demonstrated the inherent friction of the inerter plays an important role in vibration suppression and energy dissipation. Effects of friction subjected to different external forces on the effectiveness of the NFI-VIS are studied systematically using the harmonic balance method. The Coulomb friction model is used to model the inherent friction of inerters. The alternate-frequency-time (AFT) technique and numerical integration method are used to obtain the dynamic response and performance indices. In Sec. 2, models of frictional inerter-based systems are presented. The power flow analysis method is introduced, and the performance indices of the system are defined in Sec. 3. The performance of SDOF and 2DOF NFI-VIS is examined in Sec. 4. Effects of the friction of inerters on the vibration transmission and power dissipation are also presented.

2 Dynamic models

2.1 Inerter with inherent dry friction

There are various ways to realize mechanical inerters by using mechanisms such as ball-screw, rack-and-pinion, helical fluid, hydraulic systems, and living hinges [31]. Fig. 1(a) shows a schematic of a ball-screw inerter, which consists of a flywheel coupled to the ball nut, a ball screw, a radial bearing, a housing, and other components. The ball screw can convert the linear motion between two terminals (A and B) into the rotation of the ball nut and the flywheel. In this process, the ball screw and bearing provide the source of friction. Fig. 1(b) shows a rack-and-pinion inerter comprising a rack, a flywheel, a housing, pinions, and gears. Axes of the gears are mounted on the housing. The rack drives the flywheel to rotate through pinions and gears, with friction effects occurring at contact interfaces with the rack moving inside the housing. Inherent friction in inerters is unavoidable and should be considered in the vibration isolation system design.

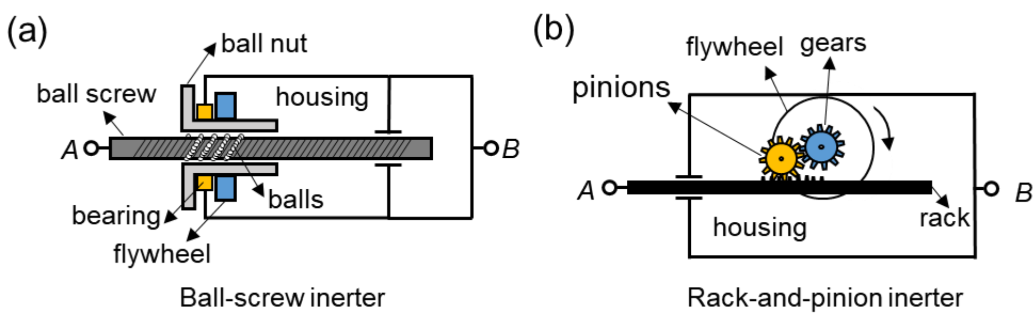

Fig. 1 Schematic drawing of (a) the ball-screw inerter and (b) the rack-and-pinion inerter.

To investigate the effects of the inherent friction of inerters, a frictional inerter model is presented and shown in Fig. 2(a). For an ideal inerter [1], the applied force f_{b} is the function of the relative acceleration of terminal A and B, i.e., $f_{\mathrm{b}} = b\ddot{x}_{\mathrm{AB}} = b(\ddot{x}_{\mathrm{A}} - \ddot{x}_{\mathrm{B}})$, where $\ddot{x}_{\mathrm{AB}}$ is the relative acceleration from terminal A to B, $\ddot{x}_{\mathrm{A}}$ and $\ddot{x}_{\mathrm{B}}$ are the accelerations, b is the inertance-mass-ratio (i.e., the apparent mass) of the inerter, in kg. Note that the actual physical mass of an inerter can be up to 2 orders of magnitude lower than that of the inertance so an ideal inerter can be considered as massless [1]. Fig. 2(b) shows the Karnopp friction model [30, 32], in which f_{d}, f_{ms} and v_{d} are the magnitudes of the dynamic friction, the maximum static friction, and the limiting velocity of the assumed zeros velocity interval $[-v_{\mathrm{d}},\ v_{\mathrm{d}}]$, respectively. In this paper, it is assumed that $f_{\mathrm{d}} = f_{\mathrm{ms}}$. Considering the frictional inerter, the applied force f_{b} is identical to the total inerter force expressed by

$$f_{\mathrm{b}}(\ddot{x}_{\mathrm{AB}}, \dot{x}_{\mathrm{AB}}) = b\ddot{x}_{\mathrm{AB}} + f_{\mathrm{bc}}, \tag{1}$$

where f_{bc} is the inherent friction force of the inerter. Clearly, f_{b} depends on the relative acceleration and velocity between the two terminals of the frictional inerter.

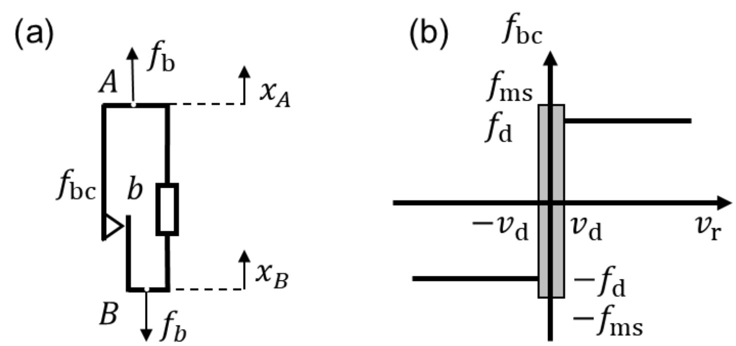

Fig. 2 Schematic representation of (a) a nonlinear frictional inerter model (b) the Karnopp model.

The use of the Karnopp model can avoid the strong nonlinearity of the classical Coulomb model at relative velocity $v_{\mathrm{r}} = 0$ considering the contact interface stuck when there is zero relative velocity [33], as shown in Fig. 2(b). This friction model is represented by

$$f_{\mathrm{bc}} = \begin{cases} f_{\mathrm{d}}\,\mathrm{sgn}(v_{\mathrm{r}}), & \text{if } |v_{\mathrm{r}}| > v_{\mathrm{d}}, \\ f_{\mathrm{ms}}\,\mathrm{sgn}(f_{\mathrm{ex}}), & \text{if } |v_{\mathrm{r}}| \le v_{\mathrm{d}} \text{ and } |f_{\mathrm{ex}}| \ge f_{\mathrm{ms}}, \\ f_{\mathrm{ex}}, & \text{if } |v_{\mathrm{r}}| \le v_{\mathrm{d}} \text{ and } |f_{\mathrm{ex}}| < f_{\mathrm{ms}}, \end{cases} \tag{2}$$

where f_{ex} and $v_{\mathrm{r}} = \dot{x}_{\mathrm{A}} - \dot{x}_{\mathrm{B}}$ are the resultant external force in the tangential direction and the relative velocity, respectively, and the signum function is defined as

$$\mathrm{sgn}(v_\mathrm{r}) = \begin{cases} \frac{v_\mathrm{r}}{|v_\mathrm{r}|}, & \text{if } |v_\mathrm{r}| \neq 0 \\ 0, & \text{if } |v_\mathrm{r}| = 0 \end{cases}. \tag{3}$$

To obtain the dynamic response, the signum function is used to express friction [34]. Based on the Coulomb friction, the inerter friction force can be approximated as $f_\mathrm{bc} \approx f_\mathrm{d}\mathrm{sgn}(v_\mathrm{r})$. For a periodic response with the relative velocity $v_\mathrm{r} \approx \hat{v}_\mathrm{s}\sin(\omega t)$, the friction force can be approximated using a fifth-order Fourier expansion as:

$$f_\mathrm{bc} \approx \frac{4f_\mathrm{d}}{\pi}\left(\sin(\omega t) + \frac{1}{3}\sin(3\omega t) + \frac{1}{5}\sin(5\omega t)\right). \tag{4}$$

Smooth regularized hyperbolic tangent function can be used to approximate the frictional force when using HB method for determining the dynamic response [35]. The friction force can be expressed by:

$$f_\mathrm{bc} = f_\mathrm{d}\tanh\left(\frac{v_\mathrm{r}}{\epsilon}\right) = f_\mathrm{d}\frac{\exp(\frac{v_\mathrm{r}}{\epsilon}) - \exp(-\frac{v_\mathrm{r}}{\epsilon})}{\exp(\frac{v_\mathrm{r}}{\epsilon}) + \exp(-\frac{v_\mathrm{r}}{\epsilon})}, \tag{5}$$

where ϵ is the tolerance parameter for the tanh regularization. Fig. 3(a) shows the time histories of the internal friction force based on the use of different models. The relative displacement between the two terminals is prescribed as $0.1\cos(\omega t)$ m. The other parameters are set as $b = 0.5$ kg, $f_\mathrm{d} = 0.04$ N, $\omega = 1$ rad/s, so that the period of the prescribed motion is $T = 2\pi/\omega = 2\pi$ s. Therefore, the figure showed 2 cycles of oscillatory motion. The figure shows that the 5$^{\text{th}}$ order Fourier expansion expression of friction force can well capture the variations of the friction force. When the smooth regularized hyperbolic tangent function as shown by Eq. (5) is used good approximation is found at a lower value of $\epsilon = 0.01$. Fig. 3(b) shows the total inerter force expressed by Eq. (1). The parameter values are set the same as those used for Fig. 3(a). The sky-blue line shows the inertance force of an ideal inerter without internal friction, i.e., $f_\mathrm{bc} =$

0. The black line represents the total inerter force for inerter with internal friction expressed by Eq. (2). The figure shows large differences in the total force inerter with and without considering friction. It shows that the presence of friction introduces strong nonlinearities into the total inerter force. There are also sudden jumps in the total force due to the change in the direction of the friction force. It is thus evident that the internal friction force can have large influence on the dynamics of systems with inerters.

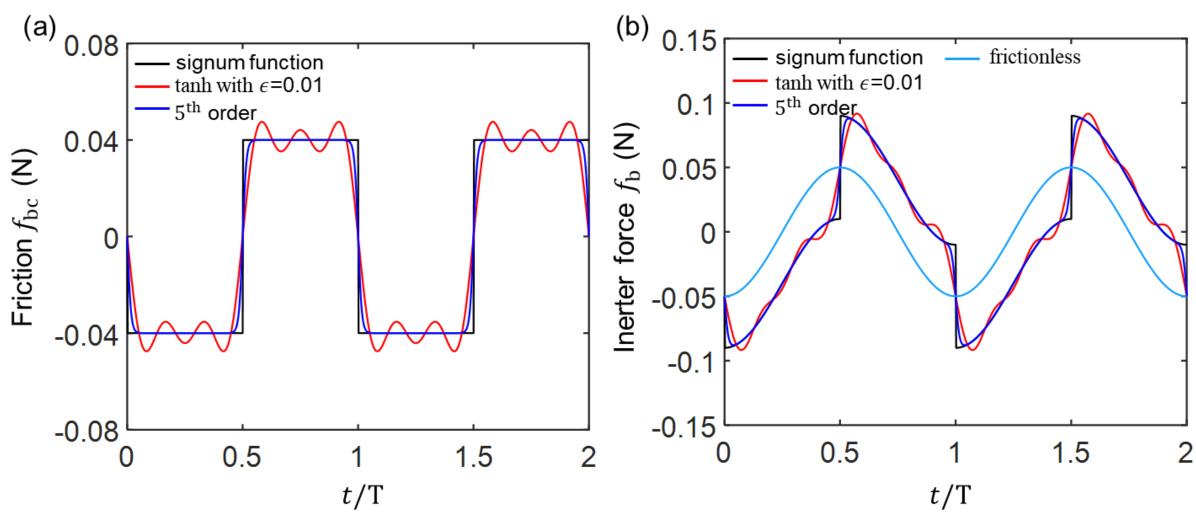

Fig. 3 Time histories of (a) the inerter friction force and (b) the total inerter force f_b based on different methods. The sky-blue line is for frictionless case. The black line is for the signum function approach, shown in Eq. (2). The blue line is for Fourier series expansion in 5th order, shown in Eq. (4). The red line is for smooth tanh-regularization methods at $\epsilon = 0.01$, shown in Eq. (5). Other parameters: $b = 0.5$ kg, $f_d = 0.04$ N, $\omega = 1$ rad/s.

2.2 Frictional inerter-based vibration isolators

In this section, three configurations for the nonlinear frictional inerter-based vibration isolators are considered in common application scenarios. The isolator composes a viscous damper with damping coefficient c, a linear spring with stiffness coefficient k, and a nonlinear inerter with inertance b and friction f_{bc}. Fig. 4(a) shows *CASE I*, in which the isolator mass m is subject to a harmonic force excitation f_e with amplitude f_0 and frequency ω. Fig. 4(b), with the model referred to as *CASE II*, is for harmonic base motion excitation case with amplitude y_0 and frequency ω. Fig. 4(c) presents a 2DOF system containing an SDOF NFI-VIS shown in Fig. 4(a) mounted on a flexible SDOF flexible base with mass m_1, spring k_1 and viscous damper c_1; this is considered as *CASE III*. Such a model can better represent the engineering applications including ship engineering and aircraft engineering. A ship structure is not rigid, and the base can be treated as a flexible foundation. The inerter is assumed to be ideal with negligible mass. The static equilibrium positions, where $x_1 = x_2 = x_3 = x_4 = 0$, of masses are set as the reference.

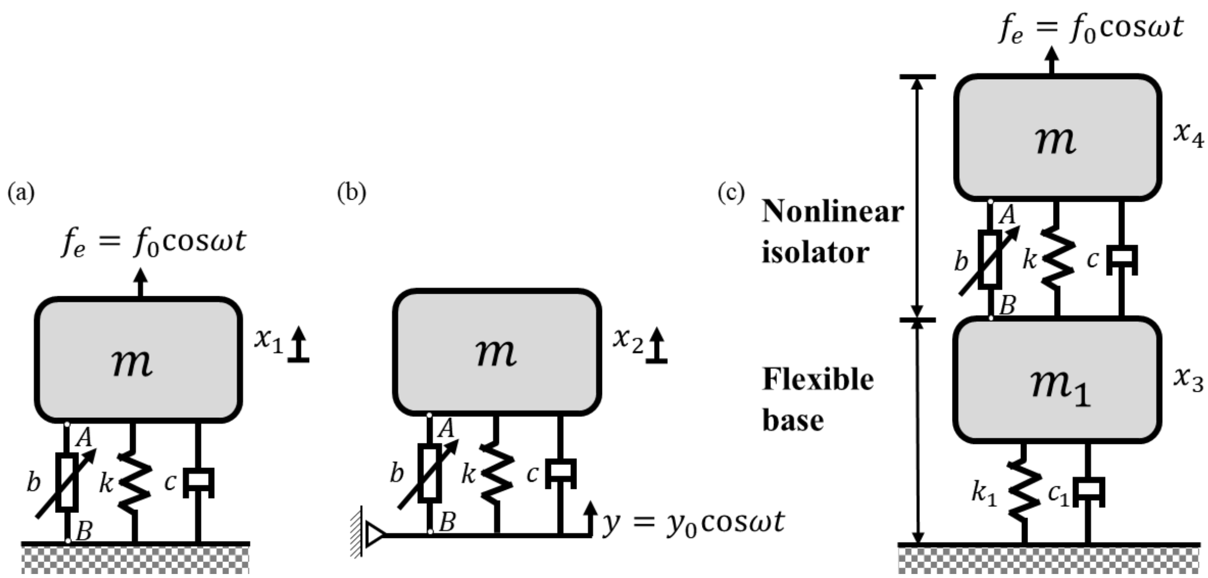

Fig. 4 Nonlinear inerter-based vibration isolators: application cases (a) SDOF NFI-VIS under force excitation (CASE I), (b) SDOF NFI-VIS under base-motion excitation (CASE II), and (c) NFI-VIS mounted on a flexible base (CASE III).

2.2.1 SDOF system (CASE I and CASE II)

For the SDOF NFI-VIS shown in Figs. 4(a) and (b), the governing equations can be expressed as:

$$m\ddot{x}_1 + b\ddot{x}_1 + c\dot{x}_1 + kx_1 + f_{\mathrm{bc1}} = f_0 \cos\omega t, \tag{6}$$

$$m\ddot{x}_2 + b(\ddot{x}_2 - \ddot{y}) + c(\dot{x}_2 - \dot{y}) + k(x_2 - y) + f_{\mathrm{bc2}} = 0, \tag{7}$$

respectively, where $f_{\mathrm{bc1}} = f(v_{\mathrm{r1}}) = f(\dot{x}_1)$, $f_{\mathrm{bc2}} = f(v_{\mathrm{r2}}) = f(\dot{x}_2 - \dot{y})$, where $y = y_0 \cos(\omega t)$. For parametric studies, the following non-dimensional parameters and variables are introduced:

$$X_1 = \frac{x_1}{l_0}, \quad X_2 = \frac{x_2}{l_0}, \quad \omega_0 = \sqrt{\frac{k}{m}}, \quad \zeta = \frac{c}{2m\omega_0}, \quad F_{\mathrm{d}} = \frac{f_{\mathrm{d}}}{kl_0}, \quad \lambda = \frac{b}{m},$$
$$F_0 = \frac{f_0}{kl_0}, \quad Y_0 = \frac{y_0}{l_0}, \quad \Omega = \frac{\omega}{\omega_0}, \quad \tau = \omega_0 t, \quad V_{\mathrm{d}} = \frac{v_d}{\omega_0 l_0}, \quad V_{\mathrm{r}} = \frac{v_r}{l_0}, \quad \sigma = \frac{\epsilon}{\omega_0 l_0}, \tag{8}$$

where l_0, X_1 and X_2 are the original length of the linear spring and the dimensionless displacement of masses in Figs. 4(a) and (b), respectively, ω_0 and ζ are natural frequencies and damping ratios, respectively, f_{d} is the magnitude of the dynamic friction, F_{d} is the non-dimensional form, λ is the inertance-to-mass ratio, F_0, Y_0, Ω and τ are the nondimensionalized force excitation amplitude, base motion amplitude, exciting frequency, and the dimensionless time, respectively, V_{d}, V_{r} and σ are dimensionless velocity dead zone, relative velocity and the tolerance ratio of tanh regularization method, respectively. Substituting parameters in Eq. (8) into Eqs. (6) and (7), following equations can be obtained:

$$X_1'' + \lambda X_1'' + 2\zeta X_1' + X_1 + F_{\mathrm{bc1}} = F_0 \cos\Omega\tau, \tag{9}$$

$$X_2'' + \lambda(X_2'' + \Omega^2 Y_0 \cos(\Omega\tau)) + 2\zeta(X_2' + \Omega Y_0 \sin(\Omega\tau)) + (X_2 - Y_0 \cos(\Omega\tau)) + F_{\mathrm{bc2}} = 0. \tag{10}$$

By introducing $Z_2 = X_2 - Y_0 \cos(\Omega\tau)$, Eq. (10) can be rewritten as

$$(1+\lambda)Z_2'' + 2\zeta Z_2' + Z_2 + F_{\mathrm{bc2}} = -Y'' = Y_0 \Omega^2 \cos\Omega\tau. \tag{11}$$

2.2.2 2DOF system (CASE III)

For the 2DOF NFI-VIS shown in Fig. 4(c), the dynamic governing equations is expressed as:

$$m\ddot{x}_4 + b(\ddot{x}_4 - \ddot{x}_3) + c(\dot{x}_4 - \dot{x}_3) + f_{\mathrm{bc3}} + k(x_4 - x_3) = f_0 \cos\omega t, \tag{12a}$$

$$m_1\ddot{x}_3 - c(\dot{x}_4 - \dot{x}_3) - k(x_4 - x_3) + c_1\dot{x}_3 + k_1 x_3 - f_{\mathrm{bc3}} - b(\ddot{x}_4 - \ddot{x}_3) = 0, \tag{12b}$$

where inherent friction $f_{\mathrm{bc3}} = f(v_{\mathrm{r3}}) = f(\dot{x}_4 - \dot{x}_3)$. Following dimensionless parameters are defined as

$$X_3 = \frac{x_3}{l_0}, \quad X_4 = \frac{x_4}{l_0}, \quad \omega_1 = \sqrt{\frac{k_1}{m_1}}, \quad \zeta_1 = \frac{c_1}{2m_1\omega_1}, \quad \mu = \frac{m_1}{m}, \quad \gamma = \frac{\omega_1}{\omega_0}, \quad \eta = \frac{k_1}{k}, \qquad (13)$$

where ω_1 and ζ_1 are natural frequencies and damping ratios of base structure, X_3 and X_4 are the dimensionless displacement of masses in Fig. 4(c), μ, γ and η are the dimensionless mass ratio, frequency ratio between the natural frequencies, and stiffness ratio, respectively. Using parameters defined in Eq. (8) and Eq. (13), Eqs. (12) can be rewritten as the following form:

$$X_4'' + 2\zeta(X_4' - X_3') + X_4 - X_3 + F_{\mathrm{bc3}} + \lambda(X_4'' - X_3'') = F_0\cos\Omega\tau, \qquad (14a)$$

$$\mu X_3'' - 2\zeta(X_4' - X_3') - (X_4 - X_3) + 2\mu\gamma\zeta_1 X_3' + \eta X_3 - F_{\mathrm{bc3}} - \lambda(X_4'' - X_3'') = 0. \qquad (14b)$$

2.2.3 Expressions of the friction force

The fourth order Runge-Kutta (RK) method is used to solve the governing equation with the friction model represented by the non-smooth signum function shown by Eq. (2). When using the seventh order HB-AFT method, the friction model with the smooth tanh function shown by Eq. (5) is used. When using the Karnopp model shown by Eq. (2), the stick phase with no relative motion between the masses is considered to be: $X_1'' = X_1' = 0$ for *CASE I*, $X_2'' - Y'' = X_2' - Y' = 0$ for *CASE II*, $X_4' = X_3'$ and $X_3'' = X_4''$ for *CASE III*. Base on the Karnopp friction model, the non-dimensional external can be denoted as: $F_{\mathrm{ex}} = F_0\cos\Omega\tau - X_1$ for CASE I, $F_{\mathrm{ex}} = Y_0\Omega^2\cos\Omega\tau - Z_2$ for CASE II, and $F_{\mathrm{ex}} = (\mu F_0\cos\Omega\tau + 2\mu\gamma\zeta_1 X_3' + \eta X_3)/(\mu + 1) - (X_4 - X_3)$ for CASE III.

3 Dynamic analysis of frictional inerter-based vibration isolation systems

3.1 Harmonic balance method

For systems shown in Fig. 4, the general equations of motion with frictional inerter-based vibration isolator can be expressed by

$$\mathbf{M}\mathbf{X}'' + \mathbf{C}\mathbf{X}' + \mathbf{K}\mathbf{X} + \mathbf{F}_{\mathrm{b}}(\mathbf{X}', \mathbf{X}'') = \mathbf{F}_{\mathrm{e}}(\tau), \tag{15}$$

where $\mathbf{M}$, $\mathbf{C}$, $\mathbf{K}$ $\in \mathbb{R}^{d\times d}$ are the mass, damping, and stiffness matrices of the corresponding linear system excluding the inerter, respectively, $\mathbf{X}$, $\mathbf{F}_{\mathrm{b}}(\mathbf{X}', \mathbf{X}'')$, $\mathbf{F}_{\mathrm{e}}(\tau)$ $\in \mathbb{R}^{d\times 1}$ are the displacement response vector, nonlinear force vector due to the inerter, and external force vector, respectively, d is the number of degrees of freedom (DOF), and the prime sign denotes derivative with respect to the non-dimensional time τ.

The steady-state periodic solution of the multiple-DOF frictional system can be achieved using the harmonic balance (HB) approach [36]. The steady-state periodic response is approximated using harmonic series. The nonlinear force terms in the governing equations are then approximated using harmonic terms with coefficients found using Fourier transform. They are then inserted into the governing equation. The coefficients of the corresponding harmonic terms with the same frequency are balanced to produce a set of algebraic equations. The solutions to these equations are then found through iterative procedures.

For low-order HB approximation, analytical derivation of the harmonic approximate expression of nonlinear term may be possible. A first-order HB approximation procedure for the NFI-VIS is shown in the appendix. For high-order HB approximation, the AFT scheme is needed, and the main idea is illustrated here with $x_{\mathrm{d}}(t)$ representing the displacement response and $f_{\mathrm{nl}}(t)$ the nonlinear force in the governing equation. In Fig. 5(a), an initial guess of the steady-state response (usually the solution of the corresponding linear system) in the time domain is denoted by $x_\mathrm{d}(t)$. Then the time histories of nonlinear force terms $f_\mathrm{nl}(t)$ in the governing equation can be obtained, as shown in Fig. 5(b). Using discrete Fourier transform (DFT), the Fourier coefficients $\tilde{H}_{(\mathrm{d,n})}$ associated with nonlinear terms $f_\mathrm{nl}(t)$ are obtained. By balancing the coefficients and solving the resultant algebraic equations using the Newton-Rapson method, a new iteration of the solution is obtained, shown by $\tilde{R}_{(\mathrm{d,n})}$ in Fig. 5(d). Note that $\tilde{R}_{(\mathrm{d,n})}$ denotes the Fourier series for the response of the d-th coordinate, which can be used to obtain the time histories $x_\mathrm{d}(t)$ of the guess for the next iteration by using inverse discrete Fourier transform (iDFT). More details on the HB-AFT method can be found in Refs. [36, 37].

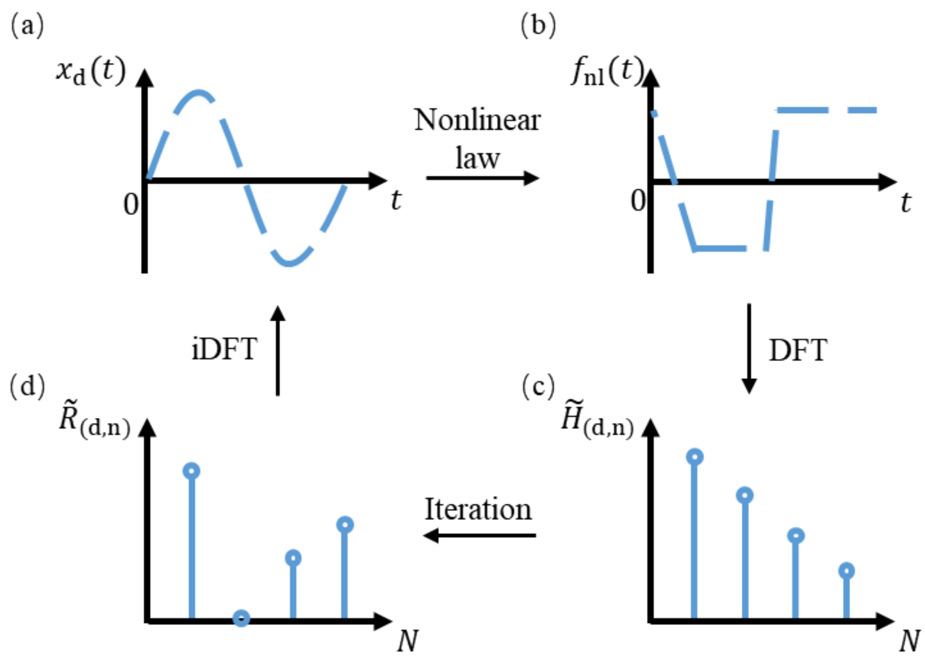

Fig. 5 Illustration of the alternating frequency-time scheme.

For Eq. (15), a truncated N-order Fourier series with a fundamental frequency Ω of approximates the steady-state displacement response $\mathbf{X}$ and the inherent friction force $\mathbf{F}_\mathrm{bc}(\mathbf{X}')$ as follows:

$$\mathbf{X} = \left\{ \sum_{n=0}^{N} \tilde{R}_{(1,n)} \mathrm{e}^{\mathrm{i}n\Omega\tau}, \ldots, \sum_{n=0}^{N} \tilde{R}_{(d,n)} \mathrm{e}^{\mathrm{i}n\Omega\tau}, \ldots, \sum_{n=0}^{N} \tilde{R}_{(D,n)} \mathrm{e}^{\mathrm{i}n\Omega\tau} \right\}^\mathrm{T}, \tag{16a}$$

$$\mathbf{F}_{\mathrm{bc}}(\mathbf{X}') = \left\{ \sum_{n=0}^{N} \tilde{H}_{(1,n)} \mathrm{e}^{\mathrm{i}n\Omega\tau}, \dots, \sum_{n=0}^{N} \tilde{H}_{(d,n)} \mathrm{e}^{\mathrm{i}n\Omega\tau}, \dots \sum_{n=0}^{N} \tilde{H}_{(D,n)} \mathrm{e}^{\mathrm{i}n\Omega\tau} \right\}, \tag{16b}$$

where $\tilde{\mathbf{R}}_{(\mathrm{d,n})}$ and $\tilde{\mathbf{H}}_{(\mathrm{d,n})}$ are the n-th order complex Fourier coefficients, which correspond to the d-th DOF, while $(\mathrm{d,n})$ represent subscripts. By differentiating Eqs. (16) with respect to time τ, it is possible to obtain the expressions for velocity $\mathbf{X}'$ and acceleration $\mathbf{X}''$. The Fourier coefficient $\tilde{\mathbf{H}}$ of the nonlinear friction force $\mathbf{F}_{\mathrm{bc}}(\mathbf{X}')$ in Eqs. (16) can be determined by using AFT technique. By inserting Eqs. (16) into the Eq. (15) and balancing the harmonic terms of the n-th order ($0 \leq n \leq N$), the following equation can be obtained:

$$(-(n\Omega)^2\mathbf{M} + \mathrm{i}n\Omega\mathbf{C} + \mathbf{K})\tilde{\mathbf{R}}_{\mathrm{n}} = \tilde{\mathbf{S}}_{\mathrm{n}} - \tilde{\mathbf{H}}_{\mathrm{n}}, \tag{17}$$

where $\tilde{\mathrm{R}}_{\mathrm{n}} = \{\tilde{R}_{(1,n)}, \dots, \tilde{R}_{(d,n)}, \dots, \tilde{R}_{(D,n)}\}^{\mathrm{T}}$, $\tilde{\mathbf{H}}_{\mathrm{n}} = \{\tilde{H}_{(1,n)}, \dots, \tilde{H}_{(d,n)}, \dots, \tilde{H}_{(D,n)}\}^{\mathrm{T}}$, $\tilde{\mathbf{S}}_{\mathrm{n}} = \{0, \dots, F_0, \dots, 0\}^{\mathrm{T}}$ for the force excitation and $\tilde{\mathbf{S}}_{\mathrm{n}} = \{0, \dots, Y_0\Omega^2, \dots, 0\}^{\mathrm{T}}$ for the base excitation. For a D-DOF system with N-th order Fourier series, $D(2N+1)$ real nonlinear algebraic equations can be established from Eq. (17) One equation is established for $n = 0$ and 2 equations are obtained for other values of n from $n = 1$ to $n = N$. These equations can then be solved by using the Newton-Raphson iterative method [10]. The analytical formulations using the first-order HB method for SDOF systems are provided in the Appendix. Note that it is possible to determine the stability of solution obtained using harmonic balance method. The Floquet theory can be used to evaluate the local stability of a periodic solution using the monodromy matrix method for time domain analysis [38], and Hill's method for analysis in the frequency domain [39, 40].

3.2 Transmissibility and power flow

3.2.1 Transmissibility

For the evaluation of vibration transfer between subsystems, force transmissibility is usually used as an index. For the SDOF system, the force transmissibility TR_{B} for the system with force excitation is defined as the ratio between the maximum transmitted force and the external force amplitude. For 2DOF systems, the force transmissibility from the primary mass m to the secondary mass m_1 can be expressed as the ratio of the maximum transmitted force to the input force amplitude:

$$TR_{\mathrm{B}} = \frac{\max(|F_{\mathrm{tB}}|)}{F_0}, \tag{18}$$

where for *CASE I* we have $F_{\mathrm{tB}} = F_0 \cos\Omega\tau - X_1''$ while for *CASE III,* we have $F_{\mathrm{tB}} = 2\zeta(X_4' - X_3') + X_4 - X_3 + F_{bc3} + \lambda(X_4'' - X_3'')$ being the non-dimensional transmitted force to mass m_1 with NFI-VIS.

The displacement transmissibility is used to evaluate the performance of the configuration for the system excited by harmonic base motion [29]:

$$DTR_{\mathrm{B}} = \frac{|X_2|}{Y_0}. \tag{19}$$

The analytical formulations of performance indices of *CASE I* and *CASE II* can also be derived using the first-order harmonic balance method shown in the appendix. The transmitted force F_{tB1}, the force transmissibility TR_{B} and the displacement transmissibility DTR_{B} can be written as:

$$F_{\mathrm{tB1}} \approx F_0 \cos\Omega\tau + \Omega^2 R_1 \cos(\Omega\tau + \theta_1), \tag{20a}$$

$$TR_{\mathrm{B}} \approx \frac{\sqrt{(F_0 + \Omega^2 R_1 \cos\theta_1)^2 + (\Omega^2 R_1 \sin\theta_1)^2}}{F_0} = \sqrt{\frac{{F_0}^2 - (2\lambda + 1)\Omega^4 {R_1}^2 + 2\Omega^2 {R_1}^2}{{F_0}^2}}, \tag{20b}$$

$$DTR_{\mathrm{B}} = \frac{|X_2|}{Y_0} \approx \frac{|X_{2\mathrm{am}}|}{Y_0} = \sqrt{1 - \left(\frac{R_2}{Y_0}\right)^2 \left(\frac{(2\lambda + 1)\Omega^2 - 2}{\Omega^2}\right)}, \tag{20c}$$

where R_1 and R_2 are dimensionless displacement amplitudes, θ_1 is the phase angle of the steady-state response of the mass m, Eqs. (32) and (38) in the Appendix were used. For an effective isolation system in terms of force transmission, $TR_{\mathrm{B}} < 1$ and $DTR_{\mathrm{B}} < 1$ are need. Therefore, we can receive the effective isolation frequency range for force and displacement transmissibility, requiring the excitation frequency to satisfy:

$$\Omega_{\mathrm{eff}} > \sqrt{\frac{2}{1+2\lambda}}. \tag{21}$$

It can be observed that the critical effective isolation frequency is the same for the two cases, depending only on the value of the inertance-to-mass ratio λ. For a conventional linear spring-mass-damper isolator, the isolation of force transmission is achieved when Ω is greater than $\sqrt{2}$. In comparison, for the NFI-VIS, increasing the value of λ broadens the effective isolation frequency range, as shown in Eq. (21). Note that when the excitation frequency tends to infinity, i.e., $\Omega \to \infty$, we have

$$TR_{\mathrm{B}\infty} = \lim_{\Omega\to\infty} TR_{\mathrm{B}} = \sqrt{1 - \frac{((2\lambda+1)\Omega^4 - 2\Omega^2){R_1}^2}{{F_0}^2}} < 1, \tag{22a}$$

$$DTR_{\mathrm{B}\infty} = \lim_{\Omega\to\infty} DTR_{\mathrm{B}} = \sqrt{1 - \left(\frac{R_2}{Y_0}\right)^2 \left(\frac{(2\lambda+1)\Omega^2 - 2}{\Omega^2}\right)} < 1. \tag{22b}$$

It is noted that when the external excitation is than the frictional force of the inerter, the inerter and system will be in the stuck mode such that the mass will be stationary. In this case, the transmitted force will be the same as the excitation force and the transmissibility will be equal to 1, meaning that the NFI-VIS will not be effective.

3.2.2 Power flow analysis

The power flow analysis is used to analyze energy transfer and for performance evaluation. The steady-state periodic response of the system is obtained through approximation of the dry friction force by using the tanh regularization [29]. The power flow variables are expressed by

$$P_{\mathrm{dv}} = \mathbf{X}'^{\mathbf{T}}\mathbf{C}\mathbf{X}', \qquad P_{\mathrm{f}} = \mathbf{X}'^{\mathbf{T}}\mathbf{F}_{\mathrm{bc}}(\mathbf{X}'), \qquad P_{\mathrm{in}} = \mathbf{X}'^{\mathbf{T}}\mathbf{F}_{\mathbf{e}}(\boldsymbol{\tau}), \tag{23}$$

where P_{dv}, P_{f} and P_{in} are dimensionless instantaneous dissipated power, friction related power, and input power, respectively. In this paper, for *CASE III*, $P_{\mathrm{dv}} = P_{\mathrm{dv1}} + P_{\mathrm{t}}$, where P_{dv1} is the instantaneous dissipated power by the viscous damper c, and P_{t} is the instantaneous transmitted power from the NFI-VIS to the base system, which is dissipated by the viscous damper c_1. It should be noted that $P_{\mathrm{dv1}} = 2\zeta X_1' X_1'$ and $P_{\mathrm{t}} = 0$ for *CASE I*; $P_{\mathrm{dv1}} = 2\zeta(X_1' - Y')(X_1' - Y')$ and $P_{\mathrm{t}} = 0$ for *CASE II*; $P_{\mathrm{dv1}} = 2\zeta(X_4' - X_3')(X_4' - X_3')$ and $P_{\mathrm{t}} = 2\mu\gamma\zeta_1 X_3' X_3'$ for *CASE III*.

For a cycle of a periodic response, the damping within the system must dissipate all of the energy input by the excitation as the total mechanical energy of the system is unchanged. In *CASE III*, the damper c_1 completely dissipates the transmitted power to the mass of base system. In this paper, time-averaged power flow variables are used:

$$\bar{P}_{\mathrm{in}} = \frac{1}{\tau_{\mathrm{p}}}\int_{\tau_{\mathrm{i}}}^{\tau_{\mathrm{i}}+\tau_{\mathrm{p}}} P_{\mathrm{in}}\mathrm{d}\tau, \quad \bar{P}_{\mathrm{dv}} = \frac{1}{\tau_{\mathrm{p}}}\int_{\tau_{\mathrm{i}}}^{\tau_{\mathrm{i}}+\tau_{\mathrm{p}}} P_{\mathrm{dv}}\mathrm{d}\tau, \quad \bar{P}_{\mathrm{f}} = \frac{1}{\tau_{\mathrm{p}}}\int_{\tau_{\mathrm{i}}}^{\tau_{\mathrm{i}}+\tau_{\mathrm{p}}} P_{\mathrm{f}}\mathrm{d}\tau\,, \tag{24}$$

where τ_{i} is the starting time for averaging, $\tau_{\mathrm{p}} = 2\pi/\Omega$ is the averaging time, $\bar{P}_{\mathrm{dv}}$, $\bar{P}_{\mathrm{f}}$ and $\bar{P}_{\mathrm{in}}$ denote the time-averaged dissipated power by the viscous damper, dissipated power by the friction and input power by the external force, respectively.

The time-averaged power dissipation ratio is determined as the share of the dissipated energy in the total input energy of the system. The time-averaged power dissipation ratios corresponding to the viscous damper and dry friction are:

$$R_{\mathrm{d}} = \frac{\bar{P}_{\mathrm{dv1}}}{\bar{P}_{\mathrm{in}}}, \qquad R_{\mathrm{f}} = \frac{\bar{P}_{\mathrm{f}}}{\bar{P}_{\mathrm{in}}}, \qquad R_{\mathrm{T}} = \frac{\bar{P}_{\mathrm{t}}}{\bar{P}_{\mathrm{in}}}, \tag{25}$$

respectively, where the power transmission ratio R_{T} represents a relative measure of vibration transmission. It indicates the proportion of the entire energy transmitted to the base through the NFI-VIS.

For the SDOF frictional inerter-based system with force excitation (*CASE I*), the analytical expressions of time-averaged power flow $\bar{P}_{\mathrm{dv}}$ and $\bar{P}_{\mathrm{f}}$ can be obtained base on Eq. (24) as

$$\bar{P}_{\mathrm{dv}} \approx 2\pi\zeta {R_1}^2\Omega, \tag{26a}$$

$$\bar{P}_{\mathrm{f}} \approx 4F_{\mathrm{d}}R_1, \tag{26b}$$

where first-order approximations of the response were used. For the base-motion excitation case (*CASE II*), the analytical results can be obtained by replacing R_1 with R_2 in Eqs. (26).

At a prescribed exciting frequency, the mass's non-dimensional maximum kinetic energy of three cases can be presented by:

$$K_{1,\mathrm{max}} = \frac{1}{2}(|X_1'|_{\mathrm{max}})^2 \approx \frac{1}{2}\Omega^2 {R_1}^2, \tag{27a}$$

$$K_{2,\mathrm{max}} = \frac{1}{2}(|X_2'|_{\mathrm{max}})^2 \approx \frac{1}{2}\Omega^2 {X_{2\_\mathrm{am}}}^2, \tag{27b}$$

$$K_{3,\mathrm{max}} = \frac{1}{2}(|X_4'|_{\mathrm{max}})^2, \tag{27c}$$

where $|X_1'|_{\mathrm{max}}$, $|X_2'|_{\mathrm{max}}$ and $|X_4'|_{\mathrm{max}}$ are the maximum dimensionless magnitudes of the velocity of the mass for three cases, respectively. The first-order approximation of the velocity was used for the approximations.

In practical applications, studies have shown the friction force is not negligible [2, 20, 24, 36]. To evaluate the magnitude of friction force as a percentage of the inertial force, we propose a friction force ratio R_{bc} to characterize the effect of friction force in the inerter, which is defined as:

$$R_{\mathrm{bc}} = \frac{\max\ (F_{\mathrm{bc}})}{\max\ (F_{\mathrm{b}})}, \tag{28}$$

where $F_{\mathrm{b}} = \lambda V_r' + F_{\mathrm{bc}}$ is the nondimensional inertance force and V_r' denotes the relative acceleration across the terminals of the inerter.

4 Results and discussion

In this section, case studies are carried out to evaluate the performance of the NFI-VIS used in different configurations. The use of NFI-VIS in SDOF models subjected to both force and motion excitation is considered in Section 4.2 and Section 4.3. Its use in the 2DOF system is then examined in Section 4.4. Throughout the paper, the order $N = 7$ is set for HB-AFT approximations with a balanced consideration of the computational accuracy and the cost.

4.1 Validation of the analysis method

In Fig. 6, the steady-state responses of the SDOF isolators obtained by different methods are presented. The solid lines denote the analytical results obtained from Eqs. (34) and (42). The dashed lines show HB-AFT approximation results, and the symbols represent these obtained using the RK method. For SDOF systems, the analytical solution, semi-analytical HB-AFT, and RK results show good agreement across the frequency range. Differences between the numerical RK and analytical HB results are due to the fact that the latter is based on a single harmonic term. From Fig. 6, it can be found that the inerter inertance can lead to the shift of the resonant frequency. In Fig. 6(b), friction leads to the occurrence of stick-slip in the low-frequency range for the base motion excitation case. This behaviour can be accurately captured by the HB-AFT and RK methods compared to the analytical HB approach (with the results denoted as Ana HB in the legend). Therefore, results shown are obtained by using the semi-analytical HB-AFT method, and RK results are provided for verification, represented by different symbols.

To ensure the functionality of the inerter in the NFI-VIS across a broad range of frequencies, three different values of the inertance-to-mass ratio λ are selected. The case with $\lambda = 0$ represents isolation systems without an inerter. By setting $\alpha_1 = F_d/F_0 = 0$ or $\alpha_2 = F_d/Y_0 = 0$, we have a frictionless system with an ideal inerter. It is noted that the analytical solution is only available for dimensionless displacements when $\alpha_1 < \pi/4$ and $\alpha_2 < \pi\Omega/4$. The values of the friction-to-excitation α_1 for the force excitation case and α_2 for the base-motion excitation case are both set to be in the range from 0.1 to 0.5, based on a previous study reported in Ref. [41].

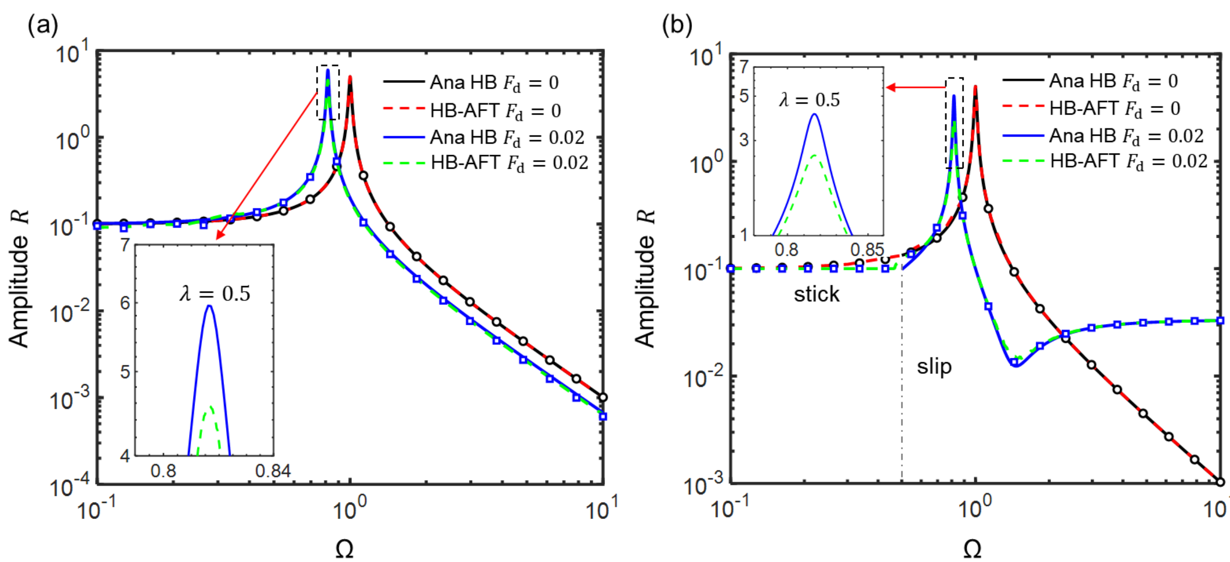

Fig. 6 Validation of the results for the SDOF NFI-VIS subjected to (a) force excitation (CASE I) and (b) base excitation (CASE II). The solid lines are the analytical HB results, and the dashed line is for HB-AFT results. RK results are shown by symbols. The black lines, red lines, and black circles are solutions of the frictionless system at $\lambda = 0$. The blue lines, green lines, and green squares are the results at $\lambda = 0.5$ and $F_d = 0.02$.

4.2 CASE I: force-excited SDOF NFI-VIS

Figs. 7 and 8 illustrate the effects of the inertance-to-mass ratio λ and the friction-to-excitation ratio α_1 on the force transmissibility TR_{B} and the maximum kinetic energy of the mass $k_{1,\max}$. λ is set at three different values for different cases, while the magnitude of the friction force F_{d} is fixed at 0.02, i.e., $\alpha_1 = 0.2$, as shown in Figs. 7(a) and 8(a). The black line represents the linear vibration isolator without inerter, i.e., $\lambda = 0$ and $\alpha_1 = 0$. The grey line represents the frictionless system inerter-based isolator based on $\lambda = 0.5$ and $\alpha_1 = 0$. The blue, red, and pink lines correspond to $\lambda = 0.5$, 1, and 5, respectively. In Figs. 7(b) and 8(b), the effects of friction force are studied by changing its magnitude from 0.02 to 0.04 at $\lambda = 0.5$ and $\lambda = 1$. The grey, blue, and cyan lines represent $\alpha_1 = 0.2$, while the red and green lines represent $\alpha_1 = 0.4$. Other parameters are fixed at $\zeta = 0.01$ and $F_0 = 0.1$.

Fig. 7(a) shows the effects of λ and α_1 on the force transmissibility TR_{B}. In Fig. 7(a), the linear spring-damper-mass isolator without inerter (i.e., $\lambda = 0, \alpha_1 = 0$) has a peak value of 50 in the force transmissibility at the frequency $\Omega = 1$. When an ideal inerter-based vibration isolator (with $\lambda = 0.5, \alpha_1 = 0$), the peak value of the force transmissibility decreases to 40.8, and an anti-peak is found. As the inertance-to-mass ratio λ increases from 0.5 to 1 and finally to 5, the peak in each curve shifts to lower frequencies. The transmissibility peak value decreases to 15.4 at $\lambda = 5$. In Fig. 7(a), the lower limit of the frequency for effective isolation is approximately 1, 0.82, and 0.43 when λ is 0.5, 1, and 5, respectively. As the excitation frequency increases, the asymptotic values of transmissibility are approximately 0.46, 0.60 and 0.86, which also can be obtained from $TR_{\mathrm{B}\infty}$ in the Eq. (22a). It shows that the resonant peak is suppressed with the increase of λ, indicating that a larger λ value provides performance benefits for the NFI-VIS. Fig. 7(b) shows the influence of the inherent friction of the inerter on the force transmissibility.

As the friction-to-excitation ratio α_1 varies from 0.2 to 0.4, the peak vibration transmission is suppressed, while the anti-peak increases slightly. When the excitation frequency continues to increase, the force transmissibility decreases firstly to a local minimum value, and then increases to an asymptotic value. However, the asymptotic value of TR_{B} increases to 0.63 at $\lambda = 0.5$ and 0.7 at $\lambda = 1$, respectively.

In Fig. 8, the effects of two parameters λ and α_1 of the NFI-VIS on the maximum kinetic energy of the mass are investigated. Three different inertance ratio values of the NFI-VIS are defined as $\lambda =$ 0.5, 1, and 5 with $\alpha_1 = 0.2$. The conventional vibration isolator without an inerter and a frictionless inerter-based vibration isolator are studied for comparison. Fig. 8(a) shows that the principal impact of introducing an ideal frictionless inerter to the vibration isolator is a modification of the resonant frequency. However, the use of a frictional inerter in the isolator can suppress the peak values of $K_{1,\max}$ from 12.3 to 6.9. Peaks of $K_{1,\max}$ shift to a lower frequency range with the increase of λ. Compared with TR_{B} curves, there is only one peak in each curve of $K_{1,\max}$. In the low-frequency range, curves tend to merge as the exciting frequency Ω decreases. At high excitation frequencies, a larger λ will result in the lower maximum kinetic energy for the primary mass. Fig. 8(a) also shows that NFI-VIS can provide improved vibration suppression performance compared to a conventional vibration isolator, i.e., $\lambda = 0$. The influence of the inerter friction is studied by varying the friction-to-excitation ratio α_1 from 0.1 to 0.5, at $\lambda = 1$ shown in Fig. 8(b). The friction can significantly reduce the peak value of the $K_{1,\max}$ over a wide frequency range, specifically at high frequencies. The reason is that the higher frequency leads to a lower dynamic response in the steady-state motion. It can be concluded from Fig. 8 that a larger value of λ and α_1 can enhance vibration isolation since it can result in a smaller amount of $K_{1,\max}$ at high exciting frequencies. The difference between HB and numerical RK results arises from the occurrence of the stick-slip phenomenon in the low-frequency range.

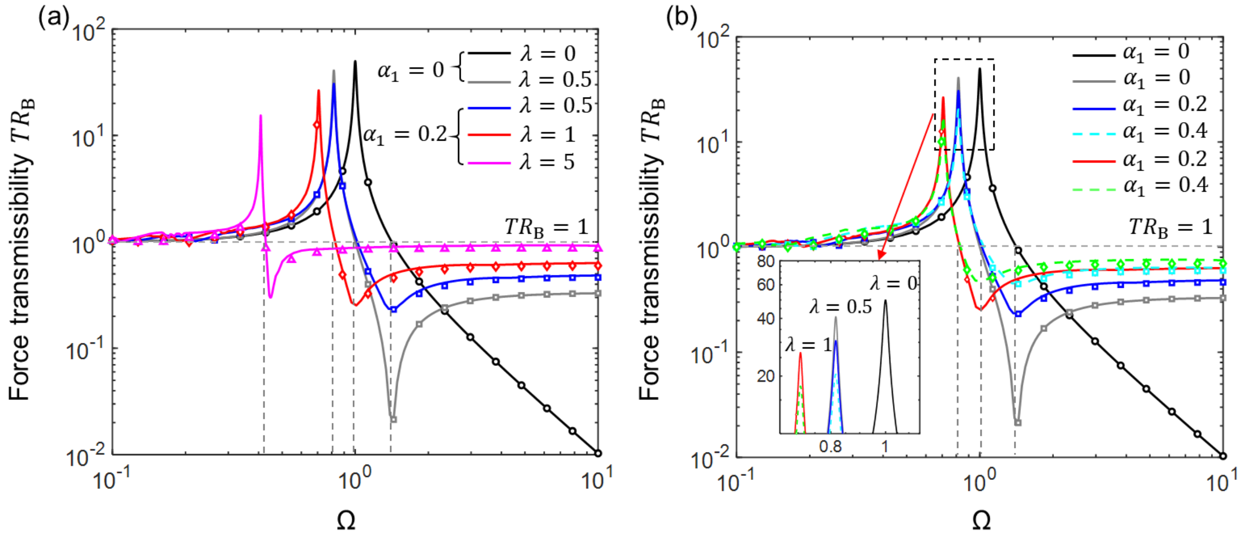

Fig. 7 Effects of the (a) inertance-to-mass ratio λ and (b) friction-to-excitation ratio α_1 on the force transmissibility TR_B of the system. The black and grey lines for the frictionless system at $\lambda = 0$ and $\lambda = 0.5$. The blue, red, and pink lines for $\lambda = 0.5$, 1, and 5 while $\alpha_1 = 0.2$, respectively. The dashed cyan and green lines for $\lambda = 0.5, 1$ with $\alpha_1 = 0.4$. Symbols: RK results. The line and symbols are colored the same for the same case.

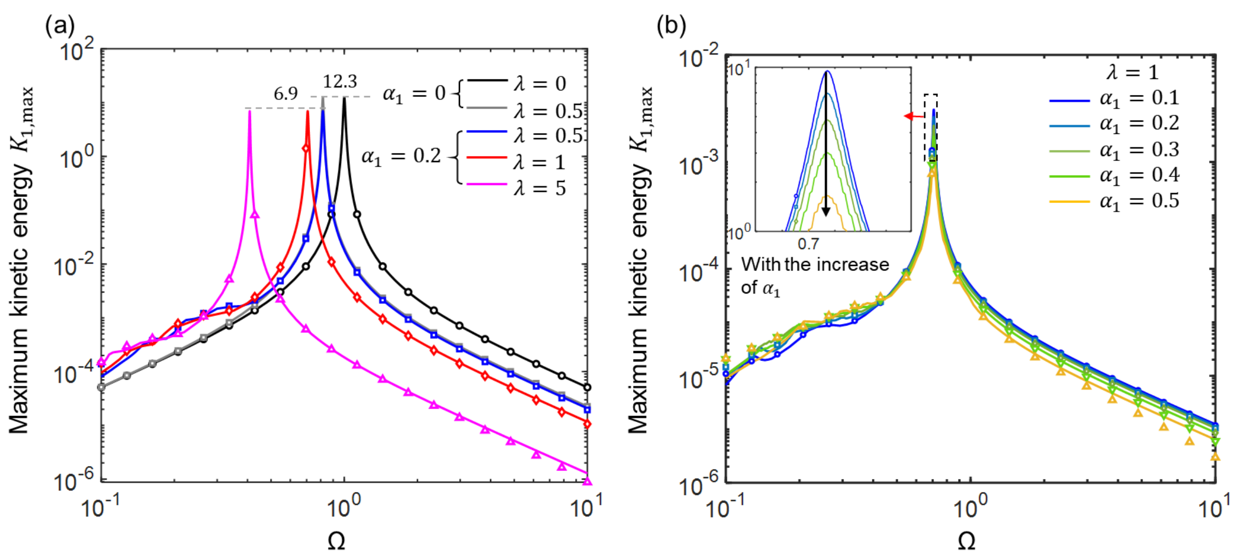

Fig. 8 Effects of the (a) inertance-to-mass ratio λ and (b) friction-to-excitation ratio α_1 on the max kinetic $K_{\max}$ of the mass. The black and grey lines for the frictionless system at $\lambda = 0$ and $\lambda = 0.5$. The blue, red, and pink lines for $\lambda = 0.5$, 1, and 5 while $\alpha_1 = 0.2$, respectively. In Fig. 8(b), different color lines for α_1 changing from 0.1 to 0.5 at an interval of 0.1, $\lambda = 1$. Symbols: RK results. The line and symbols are colored the same for the same case.

Fig. 9 shows the effects of the inertance-to-mass ratio λ and friction-to-excitation ratio α_1 of the NFI-VIS on the time-averaged power dissipation ratio of viscous damper R_{d} and friction R_{f} of the system, respectively. Figs. 9(a) and (c) depict the percentage of viscous damping and frictional energy dissipation in the system at $\alpha_1 = 0.2$ for $\lambda = 0.5$, 1, and 5, respectively. It can be found that the maximum power dissipation ratio of the damper is 75%, and the rest of the energy, i.e., 25%, is dissipated by the friction. The increase of the inertance in the NFI-VIS does not lead to changes in the percentage of the energy dissipated by the damper and the friction. The reason is that the inertance has little effect on the term $R_1\Omega$ in Eq. (26a), which is consistent with the maximum kinetic energy $K_{1,\max}$ curves in Fig. 8. However, the inclusion of inerter in the system can shift the peak frequency of the energy dissipation curve to the low-frequency range and. It shows that over 50% of the energy is dissipated by friction in the inerter and there is only a very narrow range of frequencies in which more than 50% of the energy is dissipated by the viscous damper. Figs. 9(b) and (d) show the effects of the inerter friction with $\alpha_1 = 0.2$ and 0.4 at $\lambda = 0.5$ and 1, respectively. An increase in the value of α_1 results in the value of R_{d} at peak frequency to be reduced significantly from 75% to 48.9% while the local minimum points of R_{f} increase substantially from 25% to 51.1%. This is because the frictional suppression of the dynamic response leads to a smaller portion of energy input dissipated by the viscous damper, as shown in Fig. 10. Furthermore, the increase of the friction force further narrows the frequency range where the dissipation ratio R_{d} exceeds 10%, while the frequency range of $R_{\mathrm{f}} > 90\%$ is expanded. The friction power dissipation ratio R_{f} has a local minimum point at the resonant frequency and becomes approximately close to 100%, when away from the resonant frequency. This behaviour shows that the inerter friction is effective in energy dissipation. When the magnitude of the friction force increases to 0.04, i.e., $\alpha_1 = 0.4$, damping dissipation ratio R_{d} is always less than 50.

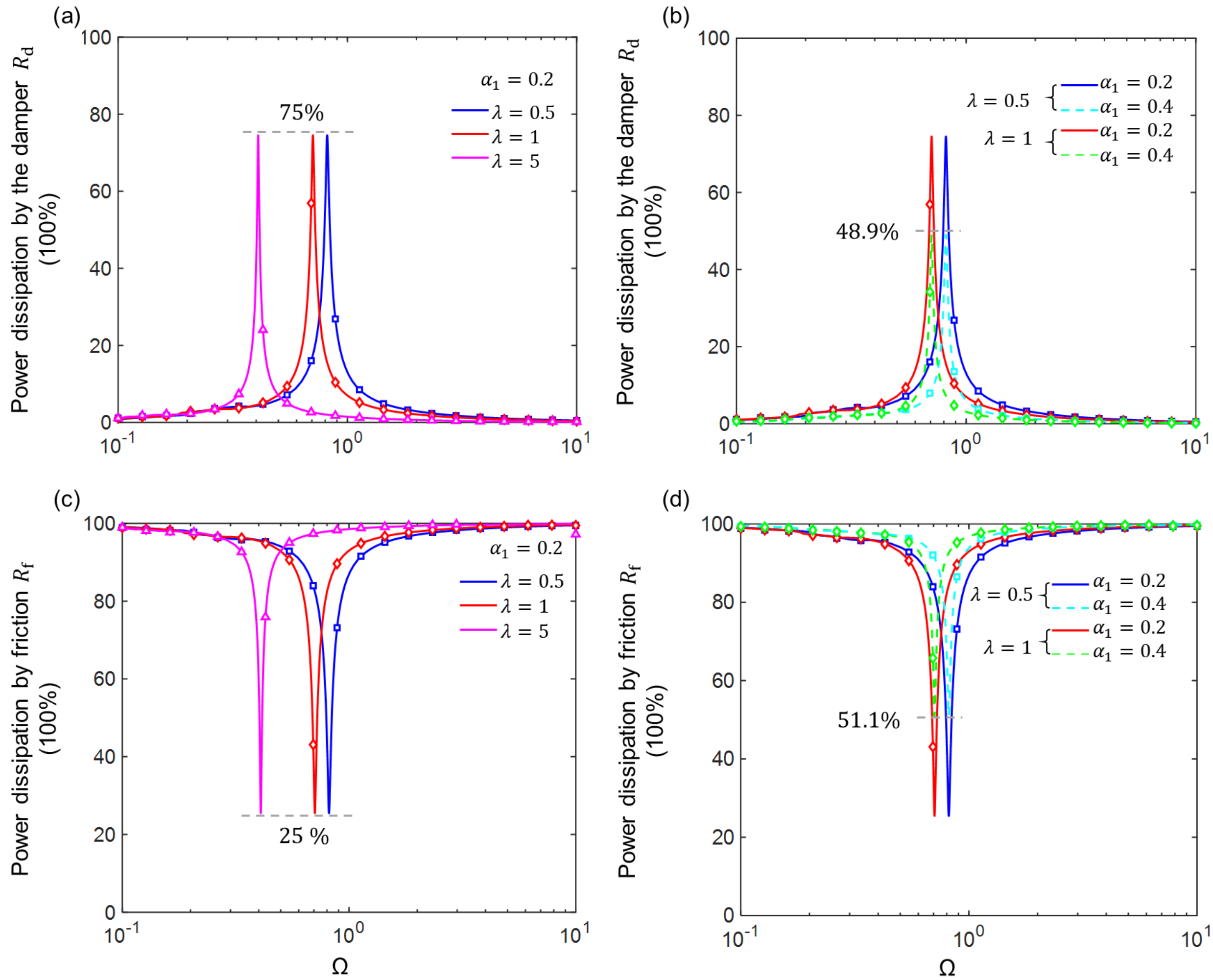

Fig. 9 Effects of the (a) inertance-to-mass ratio λ and (b) friction-to-excitation ratio α_1 on the power dissipation of the system. The blue, red, and pink lines for $\lambda = 0.5$, 1, and 5 while $\alpha_1 = 0.2$, respectively. The dashed cyan and green lines for $\lambda = 0.5, 1$ with $\alpha_1 = 0.4$. Symbols: RK results. The line and symbols are colored the same for the same case.

In Fig. 10, the time histories of the steady-state instantaneous dissipated power by damping P_{dv}, dissipated power by friction P_{f}, input power P_{in} are presented. The steady-state responses with the magnitude of friction $F_{\mathrm{d}} = 0.02$ and 0.04, $\lambda = 1$ are also shown. The excitation frequency is fixed at $\Omega = 0.5$ while other system parameters remain the same as those used for Fig. 9. Figs. 10(a) and (b) show that in the low-frequency range, an increase in friction has low impact on the power dissipated by viscous damping but results in a significant increase in frictional power dissipation. The power input of the system increases significantly with the friction increasing, as shown in Fig. 10(c). It shows that the dry friction nonlinearity strongly affects the power flow behaviour of the system. Fig. 10(d) gives the information on the nondimensional velocity and friction response in the steady state. The black and green dashed lines represent the velocity X_1' of the mass with the friction-to-excitation ratio $\alpha_1 = 0.2$ and 0.4, respectively. It can be demonstrated that the increase of friction can reduce the amplitude of the velocity response, which is consistent with the results shown in Fig. 8(b). Furthermore, it also shows that the velocity and the friction are approximately in phase, leading to the positive power dissipation by the friction P_{f}, implying that in this system, the friction plays the dominant role of energy dissipation.

Through the above research and analysis, it is found that the inherent friction of the inerter should not be neglected because it strongly affects the dynamics of the structure and thus the vibration isolation performance of the vibration isolator. In Fig. 11, the effects of the inertance-to-mass ratio λ and the friction-to-excitation ratio α_1 on the friction force are studied. Fig. 11(a) shows the friction force ratio R_{bc} at three different values of λ with the magnitude of friction $F_{\mathrm{d}} = 0.02$. The anti-peak frequency decreases and the ratio R_{bc} is reduced with the increase of λ. The friction force ratio R_{bc} is lower than 10% near the peak frequency, but larger than 50% at low frequencies and between 50% and 10% at high frequencies. When the excitation frequency tends to infinity, R_{bc} has an asymptotic value, approximately 42.7% at $\lambda = 0.5$, 33% at $\lambda = 1$, and 23% at $\lambda = 5$. In Fig. 11(b), as α_1 increases from 0.1 to 0.5 at $\lambda = 1$, the friction force ratio R_{bc} increases over a wide frequency range. Furthermore, the friction force accounts for more than 20% of the total inerter force when Ω is away from the peak frequency.

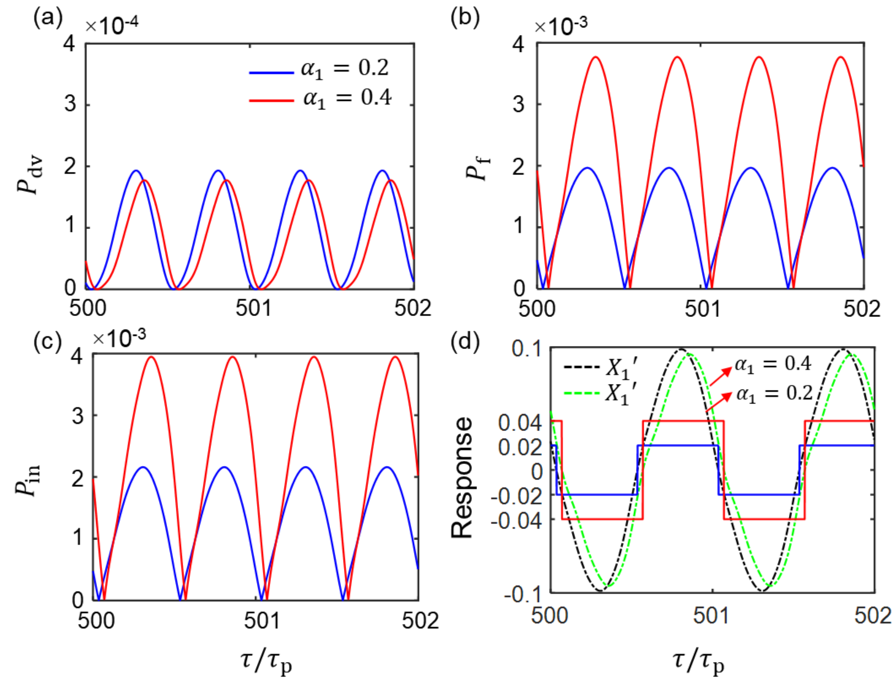

Fig. 10 Time histories of (a) instantaneous dissipated power by damping P_{dv}, (b) instantaneous dissipated power by friction P_{f}, (c) instantaneous input power P_{in} and (d) dynamic responses in the steady state at $\Omega = 0.5$ for the system with dry friction. In (a), (b), and (c), the blue and red lines are characteristics with $\alpha_1 = 0.2$ and 0.4, $\lambda = 0.5$. In (d), the blue and red lines are the dry friction force F_{d}, and the dashed black and green lines are the response velocity of the mass at $\alpha_1 = 0.2$ and 0.4, respectively.

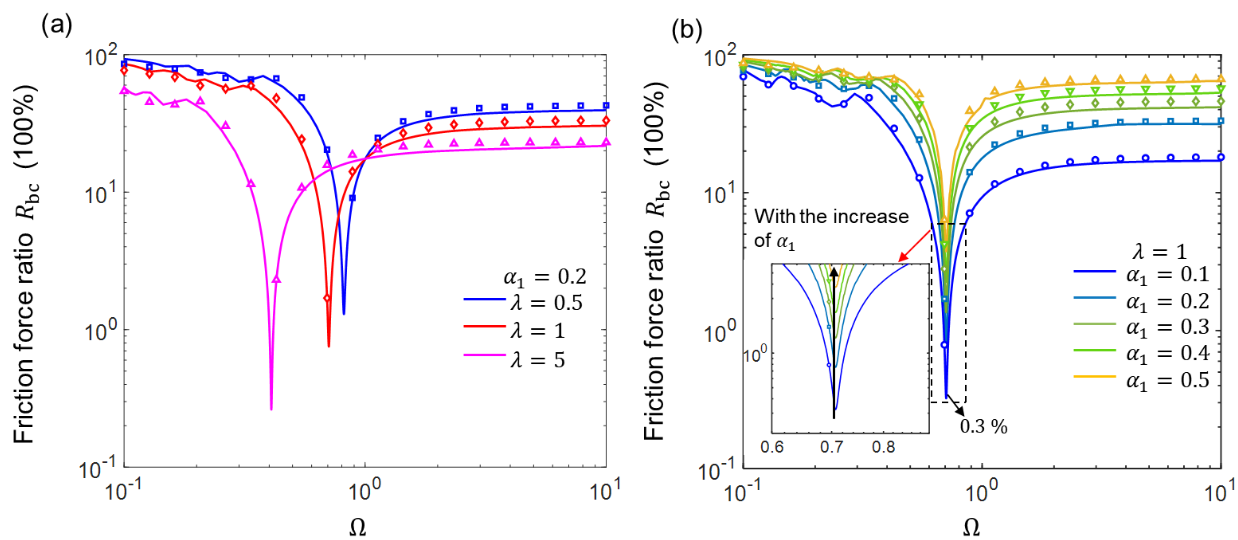

Fig. 11 Effects of the friction-to-excitation ratio α_1 on the friction force ratio R_{bc} of the inerter. The blue, red, and pink lines for $\lambda = 0.5$, 1, and 5 while $\alpha_1 = 0.2$, respectively. In Fig. 11(b), different colour lines for $\alpha_1 = 0.1\sim0.5$ with $\lambda = 1$. Symbols: RK results. The line and symbols are coloured the same for the same case.

4.3 CASE II: base motion-excited SDOF NFI-VIS

Figs. 12 and 13 show the effects of the inertance-to-mass ratio λ and the friction-to-excitation ratio α_2 on the displacement transmissibility DTR_{B} and the maximum kinetic energy $k_{2,\max}$ of the mass for the system subjected base motion excitation, respectively. Figs. 12(a) and 13(a) demonstrate the influence of λ at 0, 0.5, 1, and 5, while $\alpha_2 = 0$ and 0.2. The black line represents the conventional spring-damper-mass isolator with $\lambda = 0$ and $\alpha_2 = 0$, the black and grey lines are for isolators with an ideal inerter without friction. Figs. 12(b) and 13(b) show the influence of the friction inside the inerter with the friction level represented by α_2. Other parameters are set as $\zeta = 0.01$ and $Y_0 = 0.1$. The 7^{th} order HB-AFT approximation results shown with different lines and numerical results shown with different types of symbols by using the RK method are presented.

In Fig. 12(a), the black line shows the displacement transmissibility characteristics of the linear vibration isolator with a peak value $DTR_{\mathrm{B}} = 50$, while the grey line represents the vibration isolator with an ideal inerter, resulting in a lower peak value of $DTR_B = 40$ and an inverse peak. With an inherent friction coefficient of $\alpha_2 = 0.2$, increasing the inertance-to-mass ratio λ from 0.5 to 1, and then to 5, results in a reduction of the critical starting frequency of effective isolation (Eq. (21)), where $DTR_{\mathrm{B}} < 1$, from 1 to 0.82, and then to 0.43. At $\lambda = 5$, DTR_{B} of the NFI-VIS remains smaller than 1 in a wide frequency range. According to Eq. (22b), at high frequencies, a larger inertance-to-mass value results in a higher level of displacement transmissibility, which is consistent with the observation in Fig. 12(a). Fig. 12(b) shows that the friction force at $\alpha_2 = 0.4$, can reduce the peak in DTR_{B} curves for $\lambda = 0.5$ and 1. A stuck phenomenon occurs causing the peak frequency to shift to the right, for the case with $\alpha_2 = 0.4$ and $\lambda = 1$, due to larger inertial force. Similar to the motion characteristics due to force excitation, increasing the inertance can broaden the frequency range of the effective isolation and lower the peaks of the transmissibility curve.

Fig. 13 shows that there is an anti-peak in the curve of $K_{2,\max}$ when $\lambda = 0.5$ or 1. The peak frequency of $K_{2,\max}$ becomes lower and the peak value decreases as λ increases. At a prescribed high exciting frequency, the maximum kinetic energy increases with λ. At low excitation frequencies, the parameter λ and α_2 both have weaker effect on $K_{2,\max}$ as the curves for different cases merge. By increasing the friction-to-excitation ratio α_2 from 0.1 to 0.5, the effects of friction force are depicted in Fig. 13(b). The peak and anti-peak frequencies of $K_{2,\max}$ both increase. Compared with the force excitation case shown in Fig. 8, it can be seen that the overall trends of the $K_{2,\max}$ curves are different for the force and base-motion excitation cases.

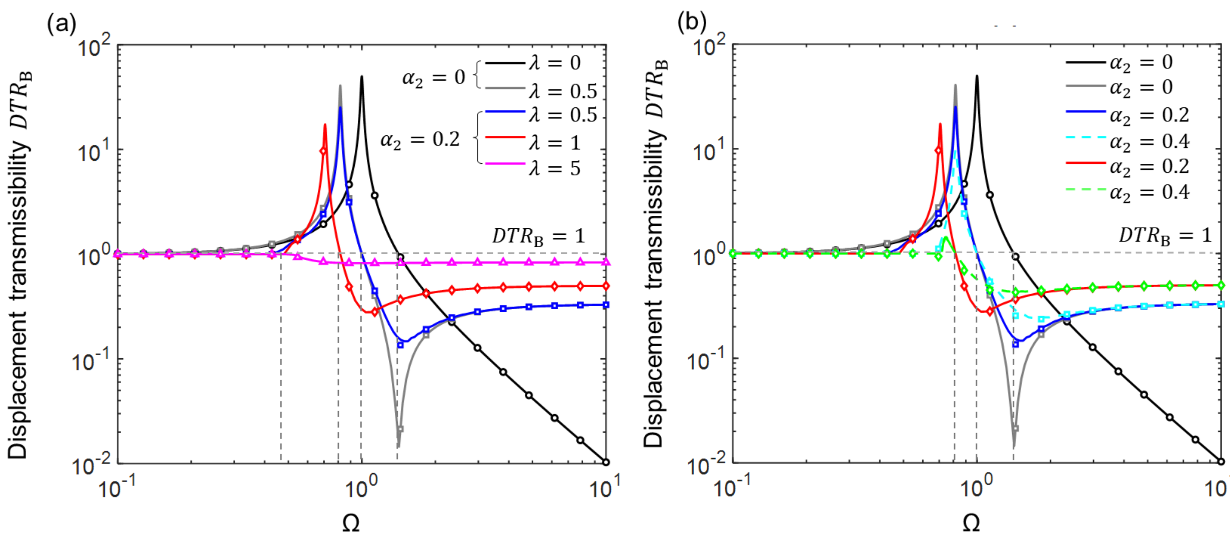

Fig. 12 Effects of the (a) inertance-to-mass ratio λ and (b) friction-to-excitation ratio α_2 on the displacement transmissibility DTR_B of the system. The black and grey lines for the frictionless system at $\lambda = 0$ and $\lambda = 0.5$. The blue, red, and pink lines for $\lambda = 0.5$, 1, and 5 while $\alpha_1 = 0.2$, respectively. The dashed cyan and green lines for $\lambda = 0.5, 1$ with $\alpha_1 = 0.4$. Symbols: RK results. The line and symbols are colored the same for the same case.

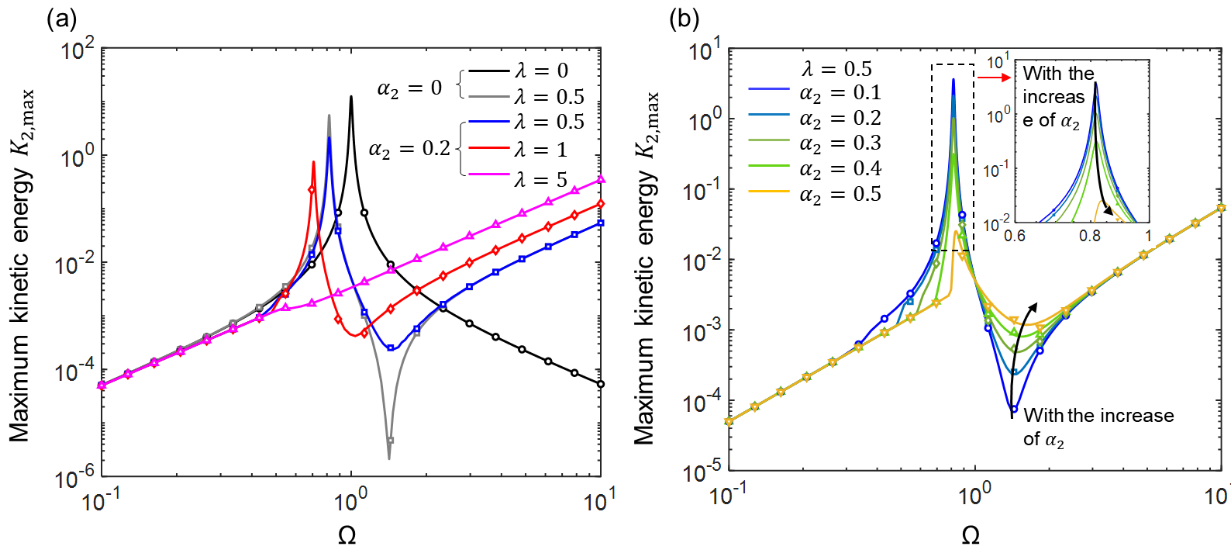

Fig. 13 Effects of the (a) inertance-to-mass ratio λ and (b) friction-to-excitation ratio α_2 on the maximum kinetic $k_{\max}$ of the mass. The black and grey lines for the frictionless system at $\lambda = 0$ and $\lambda = 0.5$. The blue, red, and pink lines for $\lambda = 0.5$, 1, and 5 while $\alpha_1 = 0.2$, respectively. In Fig. 13(b), different colour lines for α_1 from 0.1 to 0.5 with $\lambda = 1$. Symbols: RK results. The line and symbols are coloured the same for the same case.

Fig. 14 shows the effects of λ and α_2 of the NFI-VIS on the time-averaged energy dissipation of the base motion excited vibration isolator. As previously defined, R_{d} is the dissipation ratio of the viscous damper and R_{f} is the ratio of friction. Figs. 14(a) and (c) show the percentage of power dissipation by the viscous damping and friction for the system with $\lambda = 0.5$, 1, and 5 with $\alpha_2 = 0.2$. When the exciting frequency is lower than 0.5, the NFI-VIS is in a stick phase and is almost ineffective in power dissipation. At the resonant frequency, the maximum value of R_{d} is 62%, and the correspondingly R_{f} is 38%. Increasing the inertance-to-mass ratio λ causes the peak frequency to shift to lower frequencies. When $\lambda = 5$, the resonant peak disappears due to the strong inertia force. At high frequencies, R_{d} decreases, while R_{f} increases with λ. For a certain given λ, α_2 and Ω, the portion of frictional energy can be over 90% of the total energy dissipation. However, in the high-frequency range, R_{d} increases with the excitation frequency Ω. Figs. 14(b) and (d) show the effects of the friction of the NFI-VIS with $\alpha_2 = 0.2$

and 0.4 at $\lambda = 0.5$ and 1, respectively. As α_2 increases, the power dissipation ratio R_d increases significantly to the local maximum and R_f reaches the local minimum value. Increasing α_2 reduces the energy dissipation by the damper at high frequencies; this is caused by the frictional resistance. In contrast, the viscous damper of the NFI-VIS issipates energy more efficiently than the inerter friction in the high-frequency range.

To further study the power flow characteristics of the NFI-VIS under base-motion excitation, the time histories of instantaneous dissipated power of damping P_dv, dissipated power of friction P_f, input power P_in are presented in Figs. 15(a), (b), and (c), respectively. Fig. 15(d) shows the steady-state responses with the magnitude of friction force F_d being 0.02 and 0.04 while $\lambda = 1$ and $\Omega = 0.7$. The values of the remaining parameters are consistent with those used for Fig. 14. It can be found that at low frequencies, the NFI-VIS exhibits stick-slip phenomenon. The power dissipation of the damper and the friction as well as the power input reduces with the increase of the friction-to-excitation ratio α_2. In Fig. 15(d), the relative velocity $Z_2{}'$ between terminals is reduced when α_2 increases from 0.2 to 0.4 at $\Omega = 0.7$. That is consistent what is shown in Fig. 13(b) in the low-frequency range. Similarly, there is only a positive part of P_f due to the velocity and friction being of the same sign, and friction reduces the performance. Fig. 16 shows the power flow characteristics at a higher excitation frequency of $\Omega = 5$. The effects of the inertance and friction force on instantaneous power flow of damping P_dv of friction P_f and power input P_in of the system are studied. It can be concluded that in the high-frequency range, increasing the inertance will reduce the power input of the system, while increasing friction force will have the opposite effect. In Fig. 16(a), the friction-to-excitation ratio α_2 influences slightly the instantaneous power flow related to damping but significantly increases the power flow associated with friction.

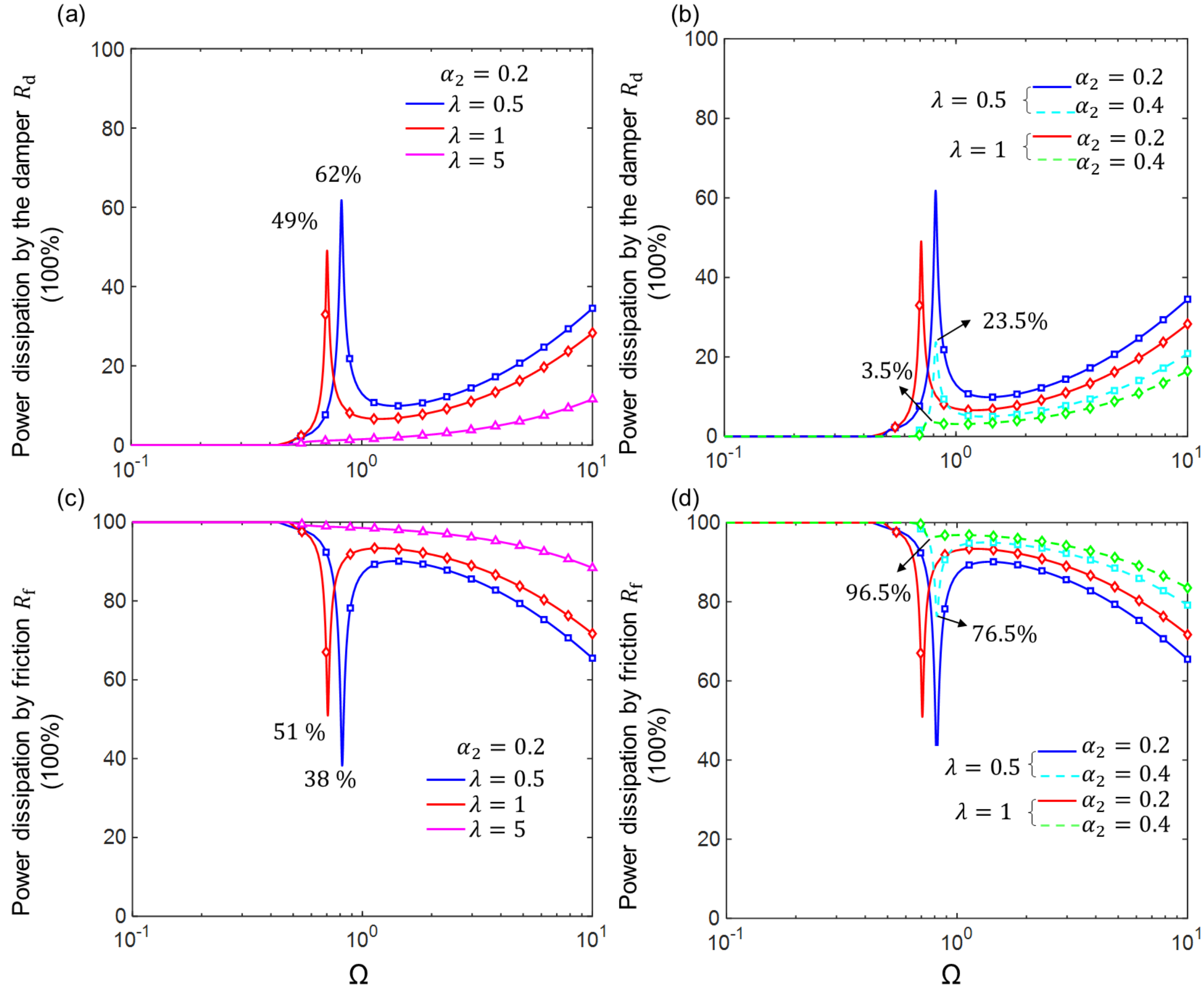

Fig. 14 Effects of the (a) inertance-to-mass ratio λ and (b) friction-to-excitation ratio α_2 on the power dissipation of the system. The blue, red, and pink lines for $\lambda = 0.5$, 1, and 5 while $\alpha_1 = 0.2$, respectively. The dashed cyan and green lines for $\lambda = 0.5, 1$ with $\alpha_1 = 0.4$. Symbols: RK results. The line and symbols are colored the same for the same case.

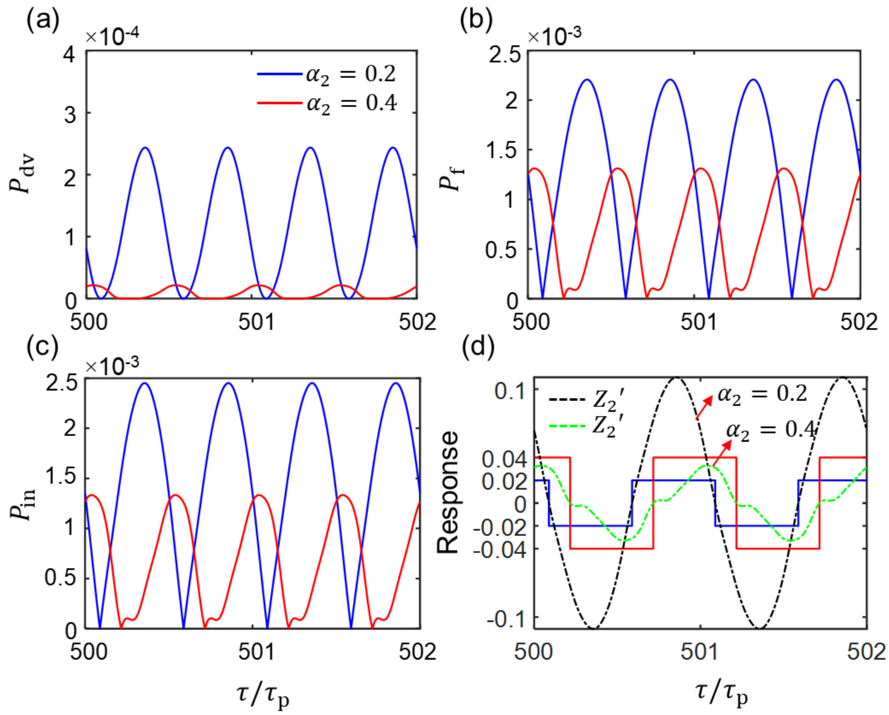

Fig. 15 Time histories of (a) instantaneous dissipated power by damping P_{dv}, (b) instantaneous dissipated power by friction P_f, (c) instantaneous input power P_{in} and (d) dynamic responses in the steady state at $\Omega = 0.7$ for the system with dry friction. In (a), (b), and (c), the blue and red lines are characteristics with $\alpha_2 = 0.2$ and 0.4 at $\lambda = 1$. In (d), the blue and red lines are the dry friction force F_d, and the dashed black and green lines are the response velocity of the mass at $\alpha_2 = 0.2$ and 0.4, respectively.

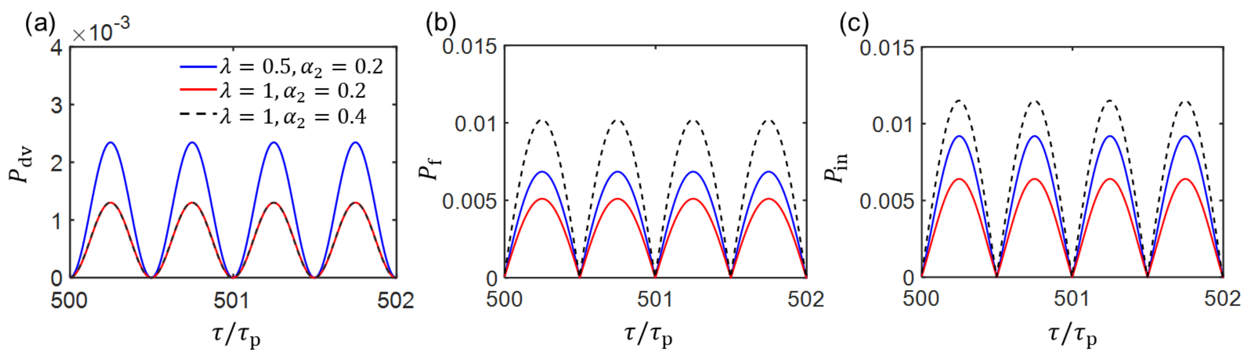

Fig. 16 Time histories of (a) instantaneous dissipated power by damping P_{dv}, (b) instantaneous dissipated power by friction P_f, (c) instantaneous input power P_{in} in the steady state at $\Omega = 5$ for the system with dry friction. The blue line is characteristic with $\alpha_2 = 0.2$ at 4 at $\lambda = 0.5$. The red line is the characteristic with $\alpha_2 = 0.2$ at 4 at $\lambda = 1$. The green line is characteristic with $\alpha_2 = 0.4$ at 4 at $\lambda = 1$.

Fig. 17 demonstrates the effects of λ and α_2 on the frictional force ratio R_{bc} for the NFI-VIS under base motion excitation. Fig. 17(a) shows the trend of the friction ratio R_{bc} with parameters set at $\alpha_2 =$

0.2, $\lambda = 0.5$, 1, and 5. It is found that when λ varies from 0.5 to 1, the local minimum of R_{bc} changes only slightly. When λ increases to 5, the anti-peak nearly disappears. In the high-frequency range, the friction force ratio R_{bc} decreases with the increase of λ and Ω. This is because the friction has relatively weak effect in the high-frequency band, as shown in Fig. 14. It is also found that R_{bc} is almost 100% in the stick phase, while R_{bc} is less than 50% in a specific wide frequency range of the slip phase. For base excitation case, increasing the value of α_2 for the inerter enlarges the percentage of friction in the inertial force, as shown in Fig. 17(b). With high-frequency excitation, the effect of friction on inertial force becomes weak due to the larger relative motion, which results in a smaller R_{bc} with the value being lower than 10%. In comparison, the friction force has a stronger effect on the dynamics of the inerter-based system when the forcing excitation away from the resonance.

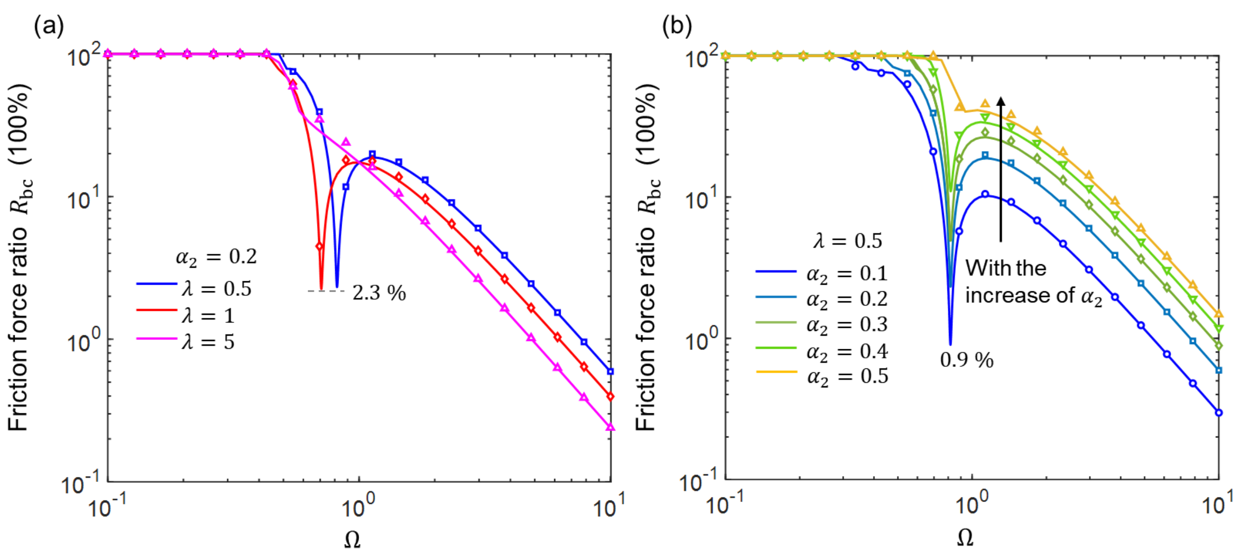

Fig. 17 Effects of the friction-to-excitation ratio α_2 on the friction force ratio R_{bc} of the inerter. The blue, red, and pink lines for $\lambda = 0.5$, 1, and 5 while $\alpha_1 = 0.2$, respectively. In Fig. 17(b), different color lines for α_1 from 0.1 to 0.5 with $\lambda = 1$. Symbols: RK results. The line and symbols are colored the same for the same case.

4.4 CASE III: 2DOF NFI-VIS subjected to force excitation

In this section, force transmission and power flow properties of the 2DOF NFI-VIS are investigated to evaluate the isolation performance. The seventh-order HB-AFT and numerical RK methods are used to obtain dynamic responses with the results shown by lines and symbols, respectively. System parameters are set as $F_0 = 0.1,\ \gamma = \mu = \eta = 1,\ \zeta = \zeta_1 = 0.01$.

Figs. 18(a) and (b) show the effects of the inertance-to-mass ratio λ and the friction-to-excitation ratio α_3 of the inerter on the relative response amplitude $|X_4 - X_3|$ between the mass m and m_1. The black line represents the conventional linear isolator case without an inerter, with two resonance peaks and one anti-resonance peak. Peaks of the relative displacement $|X_4 - X_3|$ shift to lower frequencies with the inclusion of the non-frictional inerter shown by the grey line at $\lambda = 0.5,\ \alpha_3 = 0$. When a frictional inerter with $\lambda = 0.5$ and $\alpha_3 = 0.2$ is used, the nonlinearity of the NFI-VIS becomes strong leading to peaks and a decrease in the anti-peak, as shown by the blue line. It is noted that increasing the inerter-to-mass ratio λ results in an increase in the value of first peaks and lower peak frequencies but it has a slight effect on the anti-peak at excitation frequency $\Omega \approx 1$. At high frequencies, the relative displacement decreases with the exciting frequency. Fig. 18(b) shows that as the value of α_3 increases from 0.2 to 0.4, values of $|X_4 - X_3|$ decrease, especially at high frequency. However, increasing with α_3 has weaker effect on peak frequencies. As Ω reduces in the low-frequency range, these curves tend to merge and the effects of inertance λ and friction ratio α_3 have a weak influence on the relative displacement. It is also noted that using NFI-VIS leads to a smaller peak relative response amplitude compared to a conventional spring-damper isolator with inerter, indicating the enhanced suppression by the nonlinear isolator.

Fig. 19 investigates the performance of the nonlinear isolator using the force transmissibility TR_{B2} as a performance index. Due to the frictionless inerter, the curve of TR_{B2} has two peaks and two anti-peaks compared to the conventional linear isolator case (the black curve). An increase in the frictional force of the inerter leads to the decrease of the first peak. The first peak decreases from 52.6 to 50.5 and moves to a lower frequency range as the inertance-to-mass ratio λ increases from 0.5 to 1. The curve of force transmissibility TR_{B2} shows new peaks and anti-peaks at $\lambda = 3$ and 5, resulting in lower transmitted force in a frequency range between peaks. Meanwhile, increasing λ shifts the frequency-response curve to the left, and the first peak decreases while the second increases. A larger frequency band with force transmissibility below 1 is created. The figure shows λ and α_3 have a weak effect on the anti-peaks of the force transmissibility of the system. As the value of α_3 increases from 0.2 to 0.4, the first and second peaks decrease, while the anti-peak value increases. These properties show benefits in vibration isolation using nonlinear frictional inerter. When $\Omega > 1$, TR_{B2} associated with NFI-VIS increases with Ω and approaches an asymptotic value in the high-frequency range. This value increases with α_3 and λ but remains smaller than 1. At low frequencies, the lines for different cases tend to merge.

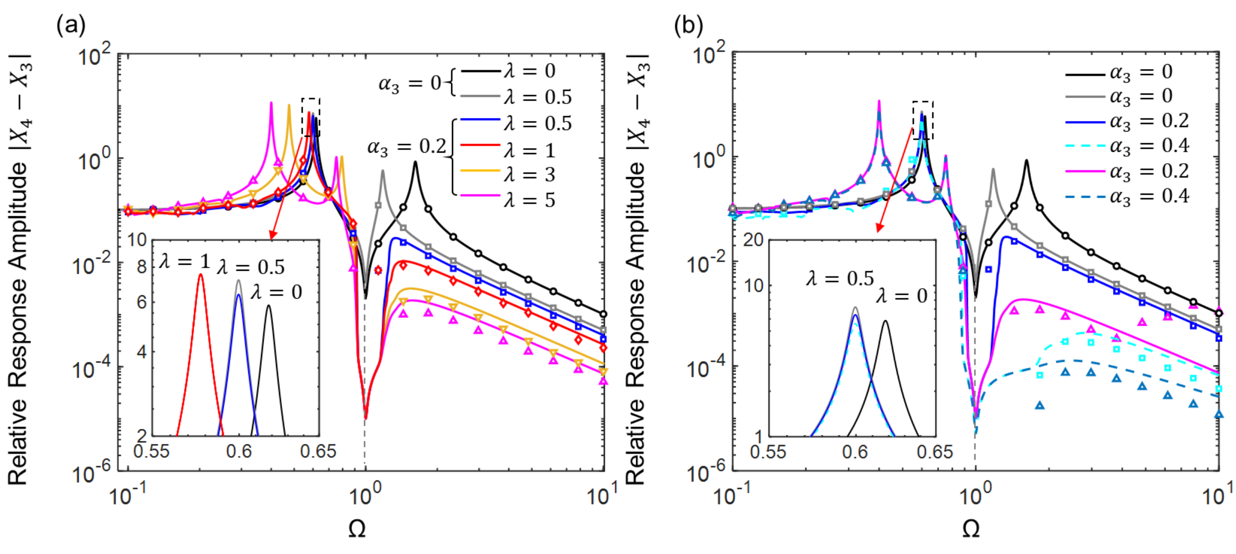

Fig. 18 Effects of the (a) inertance-to-mass ratio λ and (b) friction-to-excitation ratio α_3 on the response amplitude X_4 of m. Effects of the (a) inertance-to-mass ratio λ and (b) friction-to-excitation ratio α_3 on the relative response amplitude X_4 of m. The black and grey lines for the frictionless system at $\lambda = 0$ and $\lambda = 0.5$. The blue, red, yellow, and pink lines for $\lambda = 0.5$, 1, 3, and 5 while $\alpha_3 = 0.2$, respectively. The dashed cyan and steel-blue lines for $\lambda = 0.5, 1$ with $\alpha_3 = 0.4$. Symbols: RK results. The line and symbols are colored the same for the same case.

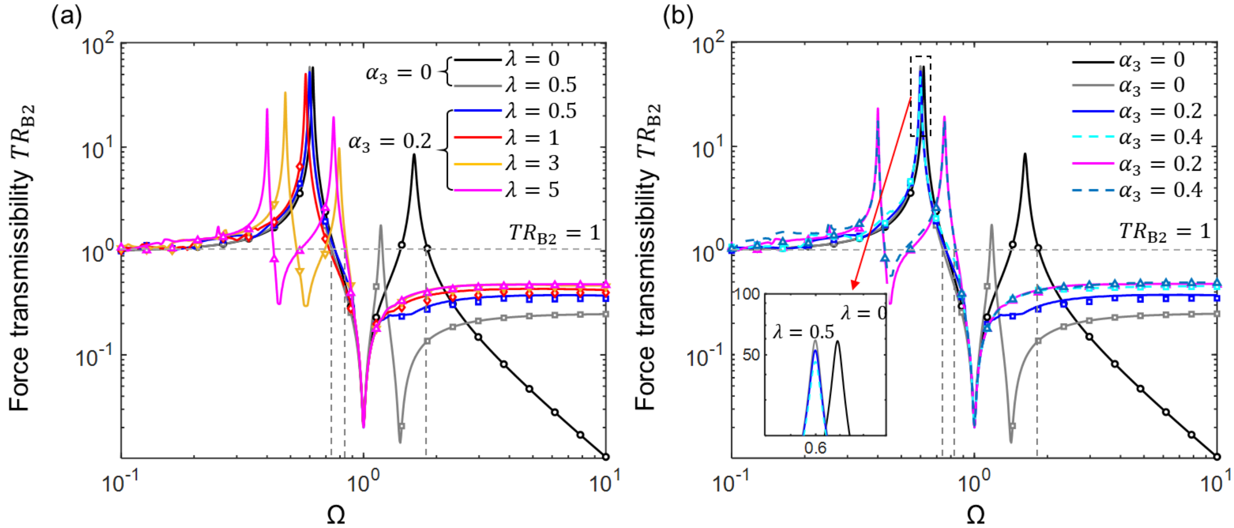

Fig. 19 Effects of the (a) inertance-to-mass ratio λ and (b) friction-to-excitation ratio α_3 on the force transmissibility TR_{B2} of the system. The black and grey lines for the frictionless system at $\lambda = 0$ and $\lambda = 0.5$. The blue, red, yellow, and pink lines for $\lambda = 0.5$, 1, 3, and 5 while $\alpha_3 = 0.2$, respectively. The dashed cyan and steel-blue lines for $\lambda = 0.5, 1$ with $\alpha_3 = 0.4$. Symbols: RK results. The line and symbols are colored the same for the same case.

Fig. 20 shows the effects of the inertance-to-mass ratio λ and the friction-to-excitation ratio α_3 on the maximum kinetic energy $K_{3,\max}$ of mass m. Fig. 20(a) shows that for the 2DOF NFI-VIS, the peak and anti-peak of $K_{3,\max}$ shift toward lower frequencies as λ increases. The first peak value of $K_{3,\max}$ decreases from 38.2 to 16.5 and the first anti-peak decrease to 3.2×10^{-4} with λ increasing from 0.5 to 5. When the excitation frequency is high, the maximum value of $K_{3,\max}$ for the NFI-VIS case is significantly lower than that for the linear isolator case (represented by the black line). These characteristics demonstrate the benefit of using the NFI-VIS for vibration isolation. In Fig. 20(b), it is shown that as α_3 increases from 0.1 to 0.5 at $\lambda = 5$, both peak and anti-peak values decrease, suggesting that friction can suppress excessive vibrations. Using a nonlinear inerter-based isolator results in a substantial decrease in the kinetic energy level of the system in the high-frequency range, which enhances vibration isolation when compared to a linear isolator.

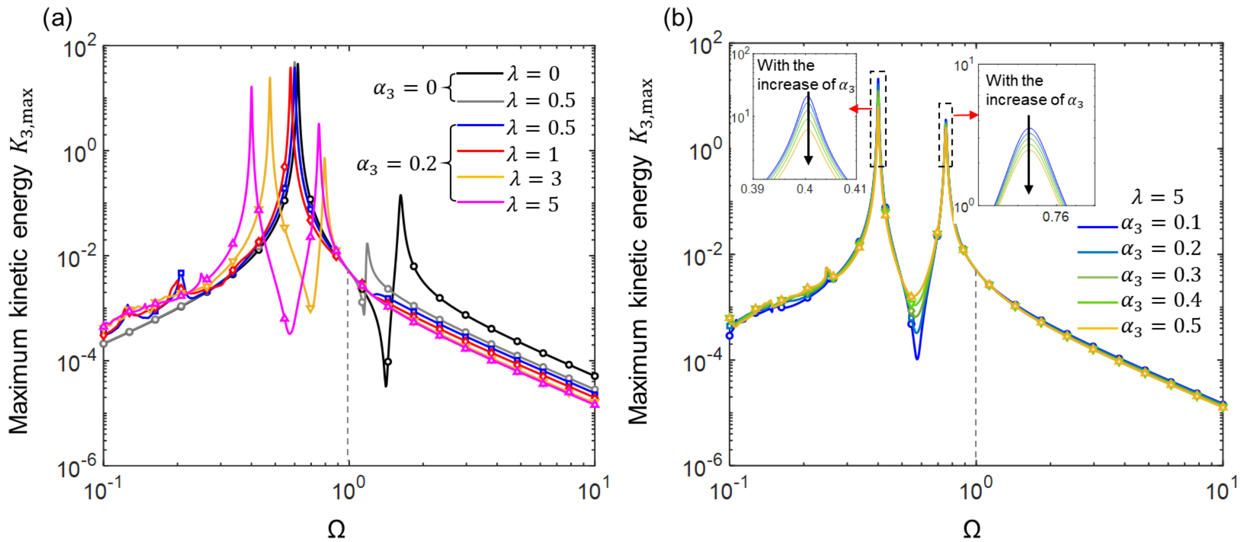

Fig. 20 Effects of the (a) inertance-to-mass ratio λ and (b) friction-to-excitation ratio α_3 on the max kinetic $K_{3,\max}$ of the mass m. The black and grey lines for the frictionless system at $\lambda = 0$ and $\lambda = 0.5$. The blue, red, and pink lines for $\lambda = 0.5$, 1, and 5 while $\alpha_3 = 0.2$, respectively. In Fig. 20(b), different colored lines for α_3 being 0.1, 0.2, 0.3, 0.4 and 0.5, with $\lambda = 5$. Symbols: RK results. The line and symbols are colored the same for the same case.

Figs. 21(a) and (b) show the effects of the inertance-to-mass ratio λ and the friction-to-excitation ratio α_3 on the time-averaged transmitted power $\overline{P}_{\mathrm{t}}$, respectively. Figs. 21(c) and (d) show the effects of λ and α_3 on the power transmission ratio R_{T}, respectively. Figs. 21(a) and (c) show that the NFI-VIS produces an anti-peak in curves of $\overline{P}_{\mathrm{t}}$, leading to a significant reduction in the transmission of vibration energy to the foundation structure. With NFI-VIS, the peak value of R_{T} is reduced as λ and α_3 increase in the low-frequency range. In the high-frequency range, R_{T} increases with λ and α_3. This observation is consistent with Figs. 23(a) and (d), where the instantaneous transmitted power P_{t} and the steady-state velocity X_3' of mass m_1 increase with friction force. Additionally, the peak value moves to lower frequencies as λ increases. In the low-frequency range, the effect of λ on $\overline{P}_{\mathrm{t}}$ becomes insignificant, as the different lines merge together. Fig. 21(d) shows that in the high-frequency range, the transmitted energy increases with the friction, as predicted in Eq. (24). The peaks and anti-peaks in the curve of R_{T} correspond to peaks and local minimum of the transmitted power $\overline{P}_{\mathrm{t}}$ of the system, as shown in Figs. 21(a) and (b). These characteristics are desirable for vibration isolation. When $\Omega \approx 1$, the transmission ratio R_{T} of the system is almost 100%, regardless of the variation of λ and α_3. This is because the system resonates at the same frequency, and the input power is almost completely transmitted to the base and dissipated by its damping.

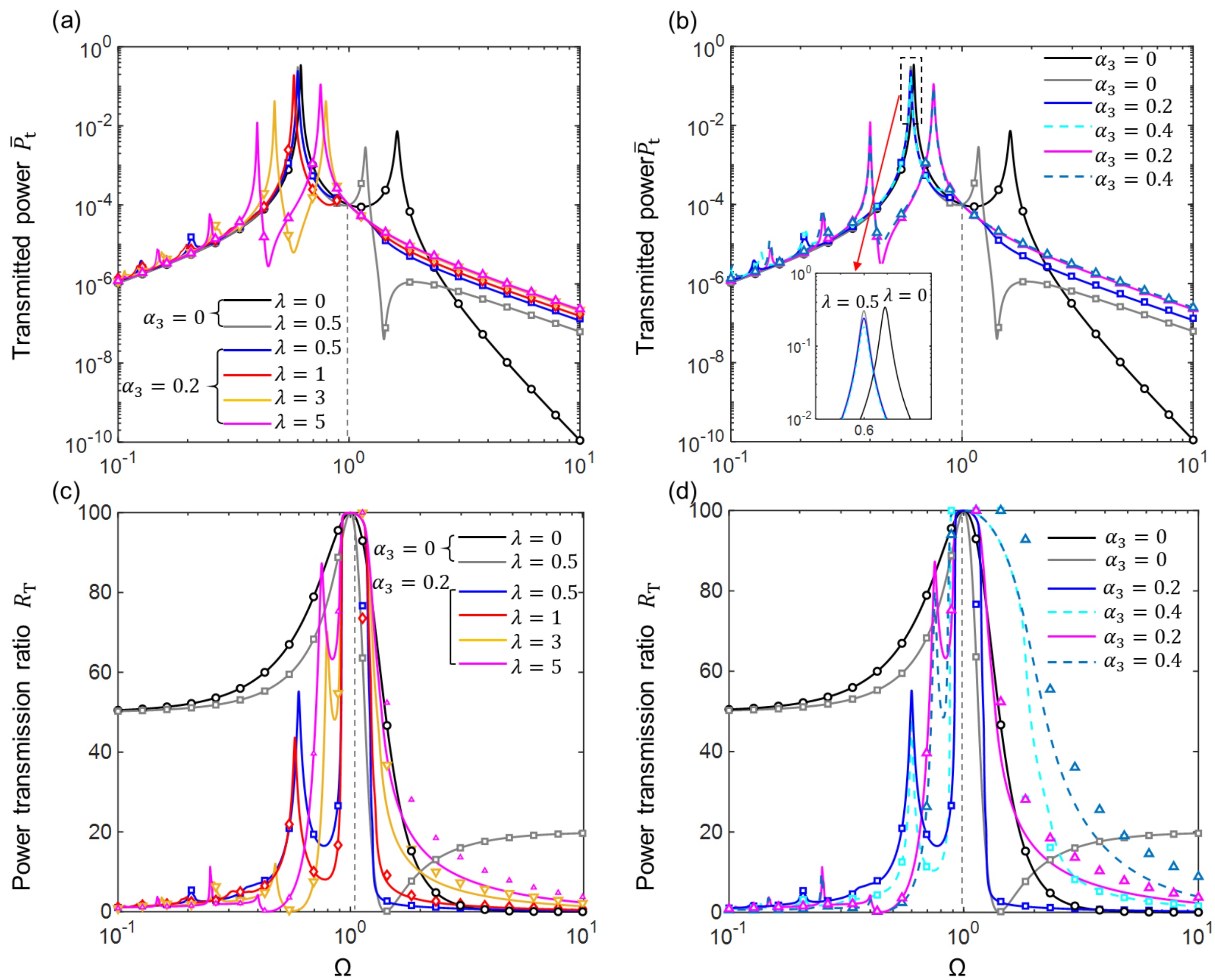

Fig. 21 Effects of the inertance-to-mass ratio λ and friction-to-excitation ratio α_3 on the (a), (c) transmitted power $\overline{P}_{\mathrm{t}}$ and (b), (d) power transmission ratio R_{T} of the system. The black and grey lines for the frictionless system at $\lambda = 0$ and $\lambda = 0.5$. The blue, red, yellow, and pink lines for $\lambda = 0.5$, 1, 3, and 5 while $\alpha_3 = 0.2$, respectively. The dashed cyan and steel-blue lines for $\lambda = 0.5, 1$ with $\alpha_3 = 0.4$. Symbols: RK results. The line and symbols are colored the same for the same case.

Fig. 22 shows the effects of λ and α_3 on the time-averaged energy dissipation of the system. Over a cycle of periodic response, the input energy of the frictionless 2DOF system is dissipated entirely by the viscous damping c and c_1. For the nonlinear structure, when $\lambda = 0.5, 1, 3$, and 5 at $\alpha_3 = 0.2$, Fig. 22(a) shows that damping c provides almost negligible energy dissipation at both low and high frequencies. This is due to the low relative velocity, indicating a small power dissipated by the damper c. Also, when Ω is away from the resonance, the transmitted energy is small. As a result, more than 90% of the input energy is dissipated by the inerter friction. Fig. 22 shows that both energy dissipation by the damping R_{d} and by the friction R_{f} increase as λ increases for the first peak when $\Omega < 1$ but decrease when $\Omega > 1$, due to the strong nonlinearity at high frequencies. Moreover, Fig. 21 demonstrates that more energy is transmitted when there is lower relative motion between the masses m and m_1. In Fig. 23, it is confirmed that the relative velocity V_{r} $(= X_4' - X_3'.)$ between the masses decreases with α_3, while the velocity X_3' of mass m_1 increases with it. At $\alpha_3 = 0.4$, the friction leads to a decrease in R_{d} and an increase in R_{f}. When $\Omega \approx 1$, the energy is entirely transferred to the base through the NFI-VIS ($R_{\mathrm{T}} \approx 1$). Therefore, it can be summarized that alterations to the friction can change the dissipation of energy within the system.

Fig. 23 shows the time histories of the power flow and response of the system at excitation frequency $\Omega = 3$ with inertance-to-mass ratio $\lambda = 5$. The instantaneous transmitted power P_{t} of damping c_1, power flow of friction P_{f}, power dissipation by the damper P_{dv1} of damping c, and steady-state responses are studied at $\alpha_3 = 0.2$ and $\alpha_3 = 0.4$, respectively. Both P_{f} and P_{dv1} decrease with the increase of friction force, while the transmitted power P_{t} increases at high excitation frequency. Corresponding to the characteristics shown in Fig. 23(d), with the increase of friction, the velocity response X_3' increases but the relative velocity V_{r} decreases. Also, the frictional power flow P_{f} (10^{-5}) and transmitted power P_t (10^{-5}) exhibit larger magnitudes than that of the damping power P_{dv1}. This is why a significant portion of the energy within the system is dissipated by the inherent friction of the inerter. Moreover, the friction has a greater effect on P_f and P_t, compared its effect on P_{dv1}. These agree with the behaviour shown in Fig. 21(d) and Fig. 22(d).

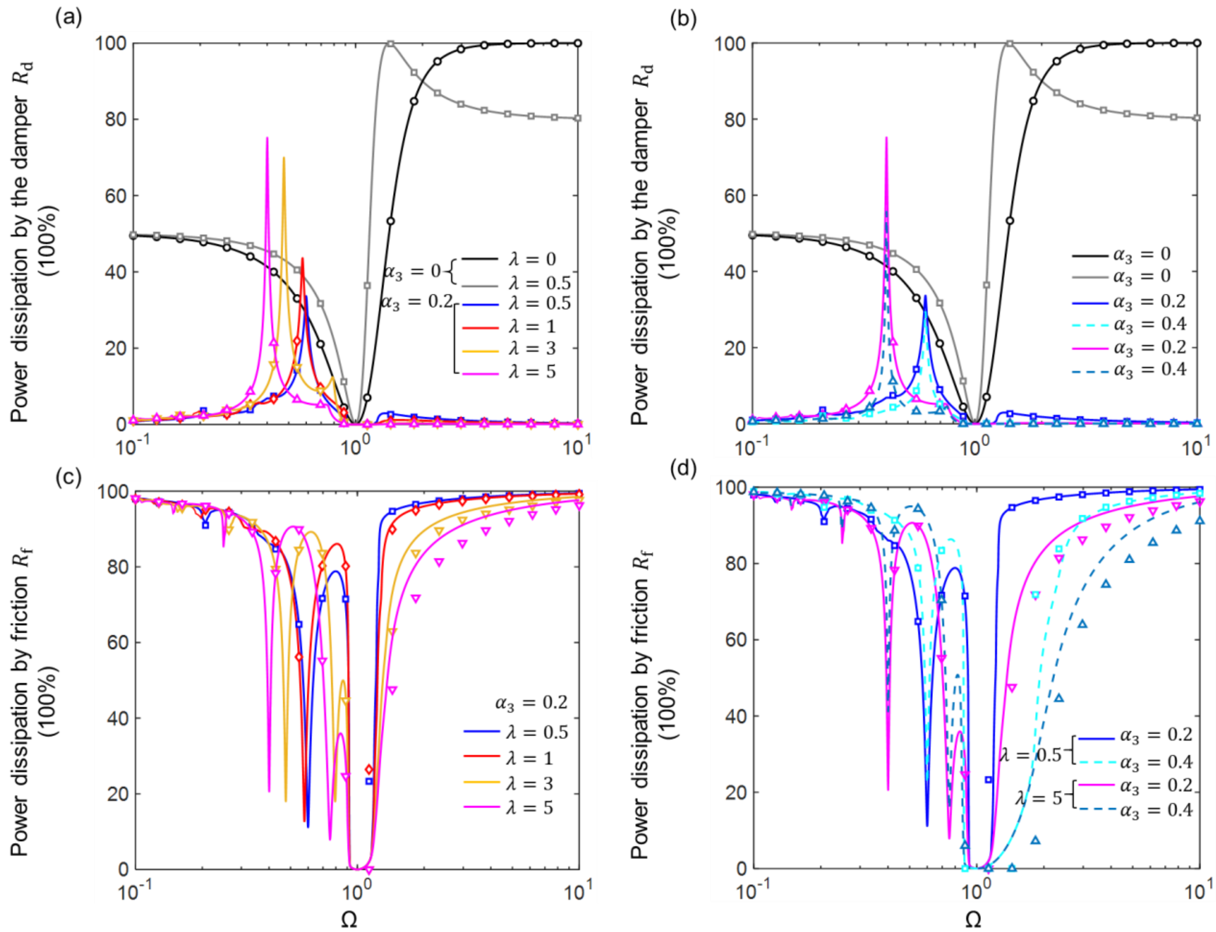

Fig. 22 Effects of the inertance-to-mass ratio λ and the friction-to-excitation ratio α_3 on the power dissipation (a) by damper R_d and (b) by friction R_f of the system. The black and grey lines for the frictionless system at $\lambda = 0$ and $\lambda = 0.5$. The blue, red, yellow, and pink lines for $\lambda = 0.5$, 1, 3, and 5 while $\alpha_3 = 0.2$, respectively. The dashed cyan and steel-blue lines for $\lambda = 0.5, 1$ with $\alpha_3 = 0.4$. Symbols: RK results. The line and symbols are colored the same for the same case.

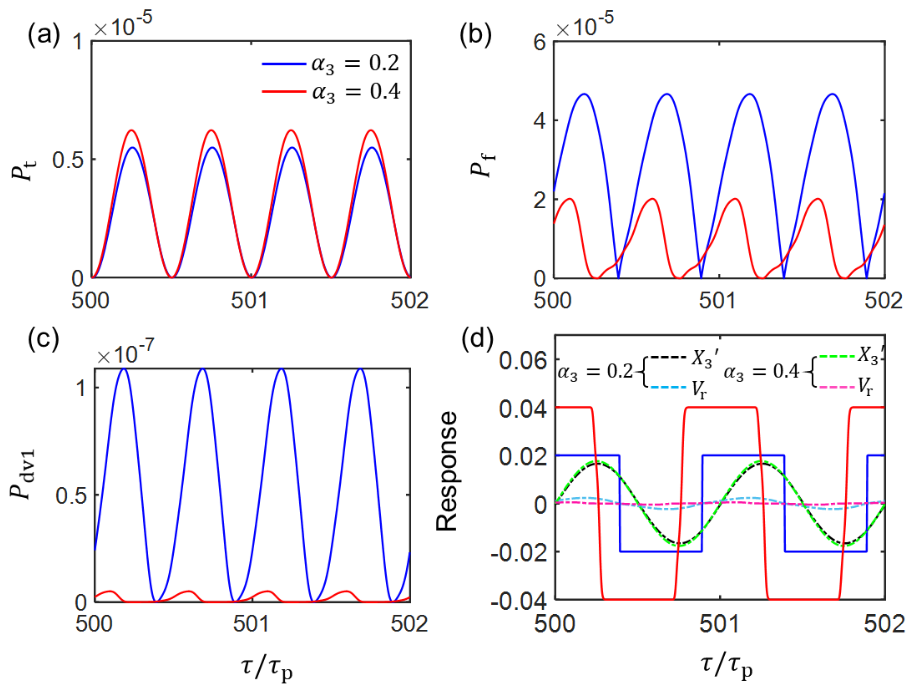

Fig. 23 Time histories of the (a) instantaneous transmitted power P_{t} (b) instantaneous dissipated power by friction P_{f}, (c) instantaneous dissipated power by damping P_{dv1}, and (d) dynamic responses in the steady state at $\Omega = 3$ for the system with dry friction. In (a), (b), and (c), the blue and red lines are characteristics with $\alpha_2 = 0.2$ and 0.4 at $\lambda = 5$. In (d), the blue and red lines are the dry friction force F_{d}, and the dashed black, green, sky-blue, and pink lines are the response velocity of the mass m_1 and relative velocity V_{r} at $\alpha_2 = 0.2$ and 0.4, respectively.

The effects of the inertance ratio λ and the friction-to-excitation α_3 on the frictional influence on the total inerter force in the 2DOF system are shown in Fig. 24. In Fig. 24(a), the consideration of the inherent friction of the inerter is essential, accounting for more than 50% of the total inerter force both in low- and high- frequency ranges. An increasing inertance-to-mass ratio λ leads to a decrease in R_{bc} and lower anti-peak frequencies. However, the value of R_{bc} increases with an increasing α_3. When $\Omega \approx 1$, R_{bc} is approximately 100%, which means $F_{\mathrm{b}} \approx F_{\mathrm{bc3}}$. This is because the mass m moving with the mass m_1 with a very small relative motion velocity ($V_{\mathrm{r}} \approx 0$), as shown in Fig. 22. When the excitation frequency $\Omega \approx \infty$, the friction force ratio R_{bc} has an asymptotic value. This is because the relative motion decreases as the exciting frequency increases, as shown in Fig. 18, indicating a smaller value of the term $\lambda V_r'$ of the inertance force F_{b}.

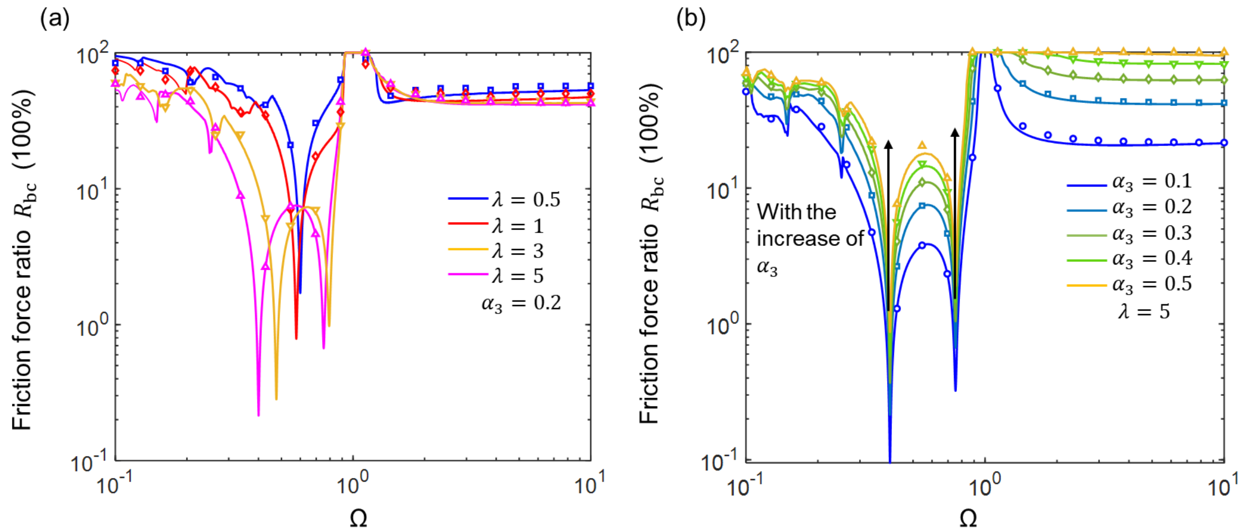

Fig. 24 Effects of the (a) inertance-to-mass ratio λ and (b) friction-to-excitation ratio α_3 on the on the friction force ratio R_{bc} of the system. The blue, red, yellow, and pink lines for $\lambda = 0.5$, 1, 3, and 5 while $\alpha_3 = 0.2$, respectively. In Fig. 24(b), different color lines for $\alpha_3 = 0.1{\sim}0.5$ with $\lambda = 5$. Symbols: RK results. The line and symbols are colored the same for the same case.

5 Conclusions

This study investigated the force transmission and power dissipation behaviour of frictional inerter-based vibration isolation systems. Different configurations of nonlinear vibration isolators with frictional inerters in single DOF and 2DOF systems under force and motion excitations were studied. The Karnopp model and the smooth friction model were used when using the HB-AFT method and numerical integration method, respectively. Vibration transmission characteristics of SDOF and 2DOF systems were shown by using force and displacement transmissibility as well as power flow variables.

For the SDOF system, the use of NFI-VIS under force (*CASE I*) and base motion (*CASE II*) excitation was studied. It is found that the inclusion of the nonlinear frictional inerter in vibration isolator can widen the effective frequency band where the force transmissibility is lower than 1. The anti-resonance in the force transmissibility and displacement transmissibility curves can be used to significantly reduce the vibration transmission at prescribed excitation frequencies. The inherent friction of inerter provides further benefits to the performance of the vibration isolator. For example, the asymptotic value of TR_{B} increases to 0.63 at $\lambda = 0.5$ and 0.7 at $\lambda = 1$ when the friction-to-excitation ratio increases from 0.2 to 0.4. Over a wide frequency range, more than 50% of the energy in the system is dissipated by the inerter friction, For the force excitation case, the friction force accounts for more than 20% of the total inerter force when the exciting frequency is away from resonance, and less than 10% near the resonant frequency. These demonstrate that it is the necessary to consider friction in inerter-based vibration isolator design. It is also noted that the NFI-VIS is only effective when the excitation amplitude is larger than the static friction of the inerter.

For the 2DOF NFI-VIS subjected to the force excitation, it is shown that the use of nonlinear frictional inerter lead to an anti-resonant peak between two peaks where the dynamic response, vibration transmission, and power transmission level is significantly reduced. With a proper design of inertance and friction in the NFI-VIS, it is possible to reduce the power transmitted ratio to nearly zero for a specific excitation frequency. This can be achieved, for example, by setting $\lambda = 5$ and $\alpha_3 = 0.4$ for low-frequency range or $\lambda = 0.5$ and $\alpha_3 = 0.2$ in the high-frequency range. When the excitation frequency is away from peak frequencies, more than 20% of the total inerter force can be caused by friction. This study showed that the internal friction of inerters should be considered in the design of inerter-based vibration isolators.

CRediT authorship contribution statement

Cui Chao: Methodology, Software, Investigation, Writing - original draft, Data curation. **Baiyang Shi**: Supervision, Writing – review & editing. **Wei Dai**: Writing – review & editing. **Jian Yang:** Conceptualization, Investigation, Supervision, Writing – review & editing, Funding acquisition.

Acknowledgment

This work was supported by the National Natural Science Foundation of China [Grant numbers 12172185, 12202152], by the Zhejiang Provincial Natural Science Foundation [Grant number LY22A020006], and by Ningbo Municipal Natural Science Foundation [Grant number 2022J174].

Statements and Declarations

Competing Interests:

The authors declare that they have no conflict of interest.

Appendix

Compared with the HB-AFT method and numerical RK method, the 1st order analytical HB approximation can be used to seek solutions providing good physical insights at low computational cost [19, 30]. For the SDOF NFI-VIS (*CASE I*), the steady-state displacement response can be approximated by

$$X_1 = R_1 \cos(\Omega\tau + \theta_1) = R_1 \cos\phi_1, \tag{29}$$

where R_1 is dimensionless displacement amplitudes and $\phi_1 = \Omega\tau + \theta_1$. The nondimensional dry friction force is expressed using harmonic terms as [30]:

$$F_{\mathrm{bc1}} \approx F_{\mathrm{d}}\, \mathrm{sgn}(X_1{}') \approx -\frac{4F_{\mathrm{d}}}{\pi}\sin\phi_1 - \frac{4F_{\mathrm{d}}}{3\pi}\sin 3\phi_1. \tag{30}$$

Substituting Eq. (30) into Eq. (9), and using $\alpha_1 = F_{\mathrm{d}}/F_0$, the steady-state frequency-response relationship can be obtained,

$$-(\lambda+1)R_1\Omega^2\cos\phi_1 - 2\zeta R_1\Omega\sin\phi_1 + R_1\cos\phi_1 - \frac{4\alpha_1 F_0}{\pi}\sin\phi_1 = F_0\cos(\phi_1 - \theta_1). \tag{31}$$

Balancing the coefficients of the associated harmonic terms, the following equations can be obtained:

$$R_1 - (\lambda + 1)\Omega^2 R_1 = F_0 \cos\theta_1, \tag{32a}$$

$$-\frac{4}{\pi}\alpha_1 F_0 - 2\zeta R_1 \Omega = F_0 \sin\theta_1. \tag{32b}$$

Eliminating the sine and cosine terms from Eqs. (32), further simplifying the equation, results in

$${R_1}^2 + (\lambda + 1)^2\Omega^4 {R_1}^2 - 2(\lambda + 1)\Omega^2 {R_1}^2 + 16\left(\frac{\alpha_1}{\pi}\right)^2 {F_0}^2 + 4\zeta^2\Omega^2 {R_1}^2 + \frac{16}{\pi}\zeta R_1 \Omega \alpha_1 F_0 = {F_0}^2. \tag{33}$$

Eq. (33) is an algebraic relationship equation of the frequency Ω and the response amplitude response R_1, for which the quadratic equation can be solved:

$$|R_1| = \frac{-\frac{16\zeta\Omega\alpha_1 F_0}{\pi} + \sqrt{\left(\frac{16\zeta\Omega\alpha_1 F_0}{\pi}\right)^2 - 4((1-(\lambda+1)\Omega^2)^2 + 4\zeta^2\Omega^2)(\frac{16(\alpha_1 F_0)^2}{\pi^2} - {F_0}^2)}}{2((1-(\lambda+1)\Omega^2)^2 + 4\zeta^2\Omega^2)}. \tag{34}$$

The following equation can be obtained:

$$\frac{|R_1|}{F_0} = \frac{-\frac{16\zeta\Omega\alpha_1}{\pi} + \sqrt{\left(\frac{16\zeta\Omega\alpha_1}{\pi}\right)^2 - 4((1-(\lambda+1)\Omega^2)^2 + 4\zeta^2\Omega^2)(\frac{16(\alpha_1)^2}{\pi^2} - 1)}}{2((1-(\lambda+1)\Omega^2)^2 + 4\zeta^2\Omega^2)}. \tag{35}$$

It is obvious that when $\frac{16(\alpha_1)^2}{\pi^2} - 1 < 0$, i.e., $\alpha_1 < \pi/4$, there exist positive and real solutions for $|R_1|/F_0$.

For the SDOF system with base motion (*CASE II*), the steady-state relative displacement's analytical first-order HB expression is

$$Z_2 = R_2\cos(\Omega\tau + \theta_2) = R_2\cos\phi_2, \tag{36}$$

where $Z_2 = X_2 - Y_0\cos(\Omega\tau)$ is the relative displacement between the mass and the base as depicted in Fig. 4(b), R_2 is dimensionless displacement amplitudes and $\phi_2 = \Omega\tau + \theta_2$. Using Flourier expression of dry friction force in Eq. (30) with $\alpha_2 = F_d/Y_0$ and substituting Eq. (36) into Eq. (10), by similar derivation approach to force excited system, following equations can be obtained:

$$F_{\mathrm{bc2}} \approx F_{\mathrm{d}}\,\mathrm{sgn}(Z_2{}') \approx -\frac{4}{\pi}\left(\sin\phi_2 + \frac{1}{3}\sin 3\phi_2\right)F_{\mathrm{d}}, \tag{37a}$$

$$-(1+\lambda)\Omega^2 R_2\cos\phi_2 - 2\zeta\Omega R_2\sin\phi_2 + R_2\cos\phi_2 - \frac{4\alpha_2 Y_0}{\pi}\sin\phi_2 = Y_0\Omega^2\cos(\phi_2-\theta_2). \tag{37b}$$

Balancing the corresponding harmonic terms in Eq. (37b), we have:

$$(1-(1+\lambda)\Omega^2)R_2 = Y_0\Omega^2\cos\theta_2, \tag{38a}$$

$$-2\zeta\Omega R_2 - \frac{4\alpha_2 Y_0}{\pi} = Y_0\Omega^2\sin\theta_2. \tag{38b}$$

Because of $\sin^2\theta_2 + \cos^2\theta_2 = 1$, Eqs. (38) can be rewritten as

$$(1-(1+\lambda)\Omega^2)^2 R_2{}^2 + \frac{16\alpha_2{}^2 Y_0{}^2}{\pi^2} + 4\zeta^2\Omega^2 R_2{}^2 + \frac{8\alpha_2 Y_0}{\pi}\zeta\Omega R_2 = Y_0{}^2\Omega^4. \tag{39}$$

The relative displacement response amplitude response R_2 can be solved by using a bisection method:

$$|R_2| = \frac{-\frac{16\zeta\Omega\alpha_2 Y_0}{\pi} + \sqrt{\left(\frac{16\zeta\Omega\alpha_2 Y_0}{\pi}\right)^2 - 4\left((1-(1+\lambda)\Omega^2)^2 + 4\zeta^2\Omega^2\right)\left(\frac{16(\alpha_2 Y_0)^2}{\pi^2} - Y_0{}^2\Omega^4\right)}}{2\left((1-(1+\lambda)\Omega^2)^2 + 4\zeta^2\Omega^2\right)}. \tag{40}$$

Similarly, it can be deduced from Eq. (40), when $\frac{16(\alpha_2)^2}{\pi^2} - \Omega^4 < 0$, i.e., $\alpha_2 < \frac{\pi\Omega}{4}$, Eq. (40) has meaningful solutions. The displacement response $X_2(\tau)$ of the mass in *CASE II* can be expressed by converting equation $Z_2 = X_2 - Y_0\cos(\Omega\tau)$:

$$X_2(\tau) = Z_2(\tau) + Y_0\cos\Omega\tau \approx R_2\cos(\Omega\tau + \theta_2) + Y_0\cos\Omega\tau. \tag{41}$$

Therefore, the dimensionless response amplitude for base excitation can be acquired by using Eqs. (38) for the simplification:

$$X_{2\_\mathrm{am}} = \sqrt{(R_2\cos\theta_2 + Y_0)^2 + R_2{}^2\sin^2\theta_2} = \sqrt{R_2{}^2 + Y_0{}^2 + 2R_2{}^2\left(\frac{1-(1+\lambda)\Omega^2}{\Omega^2}\right)}. \tag{42}$$

References

[1] Smith M.C., Wang F.C.: Performance benefits in passive vehicle suspensions employing inerters. Vehicle System Dynamics, 2004, 42(4): 235-257.

[2] Wang F.C., Hong M.F., Chen C.W.: Building suspensions with inerters. Proceedings of the Institution of Mechanical Engineers, Part C: Journal of Mechanical Engineering Science, 2010, 224(8): 1605-1616.

[3] Lazar I.F., Neild S.A., Wagg D.J.: Using an inerter-based device for structural vibration suppression. Earthquake Engineering & Structural Dynamics, 2014, 43(8): 1129-1147.

[4] Zhang S.Y., Jiang J.Z., Neild S.: Optimal configurations for a linear vibration suppression device in a multi-storey building. Structural Control and Health Monitoring, 2017, 24(3): e1887.

[5] Li Y., Jiang J.Z., Neild S.: Inerter-based configurations for main-landing-gear shimmy suppression. Journal of Aircraft, 2017, 54(2): 684-693.

[6] Smith M.C.: Synthesis of mechanical networks: the inerter. IEEE Transactions on automatic control, 2002, 47(10): 1648-1662.

[7] Salvatore A., Carboni B., Lacarbonara W.: Nonlinear dynamic response of an isolation system with superelastic hysteresis and negative stiffness. Nonlinear Dynamics, 2021: 1-26.

[8] Yang J., Jiang J.Z., Neild S.A.: Dynamic analysis and performance evaluation of nonlinear inerter-based vibration isolators. Nonlinear Dynamics, 2020, 99: 1823-1839.

[9] Szczyglowski C.P., Neild S.A., Titurus B., Jiang, J.Z., & Coetzee, E.: Passive gust loads alleviation in a truss-braced wing using an inerter-based device. Journal of Aircraft, 2019, 56(6): 2260-2271.

[10] Dong Z., Chronopoulos D., Yang J.: Enhancement of wave damping for metamaterial beam structures with embedded inerter-based configurations. Applied Acoustics, 2021, 178: 108013.

[11] Javidialesaadi A., Wierschem N.E.: Energy transfer and passive control of single-degree-of-freedom structures using a one-directional rotational inertia viscous damper. Engineering Structures, 2019, 196: 109339.

[12] Marian L., Giaralis A.: Optimal design of a novel tuned mass-damper-inerter (TMDI) passive vibration control configuration for stochastically support-excited structural systems. Probabilistic Engineering Mechanics, 2014, 38: 156-164.

[13] Lazar I.F., Neild S.A., Wagg D.J.: Using an inerter-based device for structural vibration suppression. Earthquake Engineering & Structural Dynamics, 2014, 43(8): 1129-1147.

[14] Brzeski P., Pavlovskaia E., Kapitaniak T., & Perlikowski, P.: The application of inerter in tuned mass absorber. International Journal of Non-Linear Mechanics, 2015, 70: 20-29.

[15] Li Y., Jiang J.Z., Neild S.: Inerter-based configurations for main-landing-gear shimmy suppression. Journal of Aircraft, 2017, 54(2): 684-693.

[16] Wagg D.J.: A review of the mechanical inerter: historical context, physical realisations and nonlinear applications. Nonlinear Dynamics, 2021, 104(1): 13-34.

[17] Wang Y., Li H.X., Cheng C., Ding H., & Chen L.Q.: A nonlinear stiffness and nonlinear inertial vibration isolator. Journal of Vibration and Control, 2021, 27(11-12): 1336-1352.

[18] Yang J., Jiang J.Z., Neild S.A.: Dynamic analysis and performance evaluation of nonlinear inerter-based vibration isolators. Nonlinear Dynamics, 2020, 99: 1823-1839.

[19] Papageorgiou C., Houghton N.E., Smith M.C.: Experimental testing and analysis of inerter devices. Journal of Dynamic systems, Measurement, and Control, 2009, 131(1).

[20] Wang F.C., Su W.J.: Impact of inerter nonlinearities on vehicle suspension control. Vehicle System Dynamics, 2008, 46(7): 575-595.

[21] Sun X.Q., Chen L., Wang S.H., Zhang X.L., & Yang X.F.: Performance investigation of vehicle suspension system with nonlinear ball-screw inerter. International Journal of Automotive Technology, 2016, 17: 399-408.

[22] Shen Y., Chen L., Liu Y., & Zhang X.: Modeling and optimization of vehicle suspension employing a nonlinear fluid inerter. Shock and Vibration, 2016, 2016 (5): 1-9.

[23] Brzeski P., Perlikowski P.: Effects of play and inerter nonlinearities on the performance of tuned mass damper. Nonlinear Dynamics, 2017, 88: 1027-1041.

[24] Mnich K., Lazarek M., Stefanski A., & Perlikowski P.: Identification of friction in inerter with constant

and variable inertance. Meccanica, 2022, 57(8): 1955-1973.

[25] Chao C., Shi B., Yang J., & Wiercigroch, M.: Vibration Power Dissipation in a Spring-Damper-Mass System Excited by Dry Friction. In: Dimitrovová, Z., Biswas, P., Gonçalves, R., Silva, T. (eds) Recent Trends in Wave Mechanics and Vibrations. WMVC 2022. Mechanisms and Machine Science, vol 125. Springer, Cham.

[26] Goyder H.G.D., White R.G.: Vibrational power flow from machines into built-up structures, Journal of Sound and Vibration, 1980, 68(1): 59-117.

[27] Royston T.J., Singh R.: Optimization of passive and active non-linear vibration mounting systems based on vibratory power transmission. Journal of Sound and Vibration, 1996, 194, 295–316.

[28] Yang J., Xiong Y.P., Xing J.T.: Power flow behaviour and dynamic performance of a nonlinear vibration absorber coupled to a nonlinear oscillator. Nonlinear Dynamics, 2015, 80: 1063-1079.

[29] Shi B., Dai W., Yang J.: Performance analysis of a nonlinear inerter-based vibration isolator with inerter embedded in a linkage mechanism. Nonlinear Dynamics, 2022, 109(2): 419-442.

[30] Dai W., Yang J., Wiercigroch M.: Vibration energy flow transmission in systems with Coulomb friction. International Journal of Mechanical Sciences, 2022, 214: 106932.

[31] Ma R., Bi K., Hao H.: Inerter-based structural vibration control: A state-of-the-art review. Engineering Structures, 2021, 243: 112655.

[32] Marques F., Flores P., Pimenta Claro J.C., & Lankarani H.M.: A survey and comparison of several friction force models for dynamic analysis of multibody mechanical systems. Nonlinear Dynamics, 2016, 86: 1407-1443.

[33] Karnopp D.: Computer simulation of stick-slip friction in mechanical dynamic systems. Journal of Dynamic Systems, Measurement, and Control 1985, 107: 100–103.

[34] Stein G.J., Zahoranský R., Múčka P.: On dry friction modelling and simulation in kinematically excited oscillatory systems. Journal of sound and Vibration, 2008, 311(1-2): 74-96.

[35] Pennestrì E., Rossi V., Salvini P., & Valentini P.P.: Review and comparison of dry friction force models. Nonlinear Dynamics, 2016, 83: 1785-1801.

[36] Von Groll G., & Ewins D. J.: The harmonic balance method with arc-length continuation in rotor/stator contact problems. Journal of sound and vibration, 2001, 241(2), 223-233.

[37] Cameron T. M., & Griffin J. H.: An alternating frequency/time domain method for calculating the steady-state response of nonlinear dynamic systems. Journal of Applied Mechanics, 1989, 56(1): 149-154.

[38] Peeters M., Viguié R., Sérandour G., Kerschen G., & Golinval J. C.: Nonlinear normal modes, Part II: Toward a practical computation using numerical continuation techniques. Mechanical systems and signal processing, 2009, 23(1), 195-216.

[39] Lazarus A., & Thomas O.: A harmonic-based method for computing the stability of periodic solutions of dynamical systems. Comptes Rendus Mécanique, 2010, 338(9), 510-517.

[40] Wu J., Hong L., & Jiang J.: A robust and efficient stability analysis of periodic solutions based on harmonic balance method and Floquet-Hill formulation. Mechanical Systems and Signal Processing, 2022, 173, 109057.

[41] Nayfeh A.H., Balachandran B.: Applied nonlinear dynamics: analytical, computational, and experimental methods. John Wiley & Sons, 2008.